RESEARCH ARTICLE

Correspondence to:
A. L. Lee,
earall@leeds.ac.uk

Modeling the impact of melt on seismic properties during mountain building

Amicia L. Lee[1] , Andrew M. Walker[1] , Geoffrey E. Lloyd[1] , and Taija Torvela[1]

[1]Institute of Geophysics and Tectonics, School of Earth and Environment, University of Leeds, Leeds, UK

Abstract Initiation of partial melting in the mid/lower crust causes a decrease in *P* wave and *S* wave velocities; recent studies imply that the relationship between these velocities and melt is not simple. We have developed a modeling approach to assess the combined impact of various melt and solid phase properties on seismic velocities and anisotropy. The modeling is based on crystallographic preferred orientation (CPO) data measured from migmatite samples, allowing quantification of the variation of seismic velocities with varying melt volumes, shapes, orientations, and matrix anisotropy. The results show nonlinear behavior of seismic properties as a result of the interaction of all of these physical properties, which in turn depend on lithology, stress regime, strain rate, preexisting rock fabrics, and pressure-temperature conditions. This nonlinear behavior is evident when applied to a suite of samples from a traverse across a migmatitic shear zone in the Seiland Igneous Province, Northern Norway. Critically, changes in solid phase composition and CPO, and melt shape and orientation with respect to the wave propagation direction can result in huge variations in the same seismic property even if the melt fraction remains the same. A comparison with surface wave interpretations from tectonically active regions highlights the issues in current models used to predict melt percentages or partially molten regions. Interpretation of seismic data to infer melt percentages or extent of melting should, therefore, always be underpinned by robust modeling of the underlying geological parameters combined with examination of multiple seismic properties in order to reduce uncertainty of the interpretation.

1. Introduction

Large volumes of partial melt have been suggested to exist in the middle and lower crust of orogens where they can significantly affect the crustal rheology and may enable processes such as strain localization, channel flow, melt channeling into shear zones, and postorogenic collapse [e.g., *Arzi*, 1978; *Mckenzie*, 1984; *Hollister and Crawford*, 1986; *Brown and Solar*, 1998; *Rutter and Neumann*, 1995; *Brown*, 2007; *Kohlstedt et al.*, 2009; *Sawyer et al.*, 2011; *Jamieson et al.*, 2011; *Brown et al.*, 2011]. The stability and rheology of active orogenies (e.g., Himalaya-Tibet orogen) is thought to be in part controlled by crustal melts [*Vanderhaeghe and Teyssier*, 2001a, 2001b; *Teyssier and Whitney*, 2002]. Seismology has been used to predict melt volumes in the crust and mantle in orogenic systems as well as volcanic environments [e.g., *Hirn et al.*, 1997; *Blackman and Kendall*, 1997; *Holtzman and Kendall*, 2010; *Bastow et al.*, 2010; *Cornwell et al.*, 2010]. In the melt-rich environments of mid-ocean ridges (MORs) and volcanic regimes, it has become clear that melt shape and distribution is important when predicting melt volume [*Mainprice*, 1997; *Hammond and Kendall*, 2016]. However, this type of analysis has not been applied to orogenies. Nevertheless, an assessment of the amount and distribution of melt is crucial to understand lithospheric rheology.

Orogenies are different from MORs because they are chemically more complex: metamorphic phase reactions of multicomponent Si-rich crust leads to changes in both solid and melt phase compositions, whereas in MORB melts are essentially formed by decompressional melting of peridotite. Previous studies have analytically modeled seismic velocities and anisotropies of partial melt within an isotropic matrix [e.g., *Walsh*, 1969; *O'Connell and Budiansky*, 1977; *Mavko*, 1980; *Schmeling*, 1985; *Takei and Kumazawa*, 1995; *Hammond and Humphreys*, 2000a; *Hammond and Humphreys*, 2000b; *Takei*, 2002; *Holtzman and Kendall*, 2010; *Hammond and Kendall*, 2016]. However, melting in orogens is also predicted to be syn-kinematic with deformation affecting melt shapes and distribution, and leading to crystallographic preferred orientations (CPO) of solid mineral phases. As the partitioning of stress and strain between melt and solid is uncertain, different

approximations are used to calculate seismic properties. For solid rock, seismic compressional (Vp) and shear (Vs) wave velocities and anisotropies (AVs) can be calculated from the CPO of mineral phases according to their modal proportions [*Tatham et al.*, 2008; *Lloyd et al.*, 2009, 2011a, 2011b]. Partial melts impact on these estimates [*Holtzman et al.*, 2003; *Holtzman and Kendall*, 2010], typically causing reductions in velocities [*Schilling and Partzsch*, 2001]. A further complication is that partially molten rocks are expected to behave anelastically with processes such as melt squirt leading to frequency dependent velocities (dispersion) and an intrinsic reduction in amplitudes (e.g., attenuation) [*Mavko and Nur*, 1975; *Jackson*, 2015]. Because crustal melts are orders of magnitude more viscous than MORB [*Bauchy et al.*, 2013], the anelastic relaxation of migmatites is different to MORB.

The common assumption that seismic velocities decrease linearly after the initial melting has meant that seismic methods such as Vp/Vs ratios are still often used as a tool to quantify both the size of magma chambers/partially molten volumes and/or melt percentages in various tectonic environments [e.g., *Schilling and Partzsch*, 2001; *Caldwell et al.*, 2009; *Lin et al.*, 2014]. Recent evidence, however, suggests that melt-seismic property relationships are nonlinear [*Karato*, 2010; *Hammond and Kendall*, 2016], while the effect on seismic anisotropy (AVs) remains unclear [*Xie et al.*, 2013]. In addition, different geophysical methods yield different results (e.g., the Himalayan-Tibetan system). For example, *Makovsky et al.* [1999] identified seismic bright spots from the INDEPTH profile, suggesting an "aqueous fluid" is present which could represent up to 10% melt. The Hi-CLIMB experiment, which involved an 800 km seismic array, also observed these bright spots [*Nábělek et al.*, 2009], but conclude that the low to average Vp/Vs ratio indicates absence of widespread melt beneath central to Southern Tibet. *Kind et al.* [2002] also suggest the melt is not widespread but occurs in accumulations that impact on the Vp/Vs ratio. Furthermore, as Vs are sensitive to partial melt [*Oliver*, 1962], *Caldwell et al.* [2009] suggest 3–7% melt in an upper middle crustal channel based on a 7–17% velocity decrease at 30 km depth. *Caldwell et al.* [2013] used common conversion point stacking of Ps receiver functions to identify negative impedance contrasts supporting the presence of fluid or melt in the Garhwal Himalaya.

Magnetotelluric (MT) profiles identify regions of anomalies in conductivity, with high conductivity values within the crust known to result from melt, metamorphic fluids and/or brine [*Nelson et al.*, 1996; *Wei et al.*, 2001]. *Lemonnier et al.* [1999] conclude that a high conductivity zone across the Himalaya is caused by metamorphic fluids as temperatures are insufficient to yield melt [*Henry et al.*, 1997]. Conversely, *Unsworth et al.* [2005] suggest there is an increased heat flow within the low resistivity layer, coupled with a viscosity reduction, indicating 5–14% melt beneath Southern Tibet.

In this paper, we adapt and further develop modeling methods used to estimate melt in volcanic regimes and MORs [*Mainprice*, 1997; *Holtzman and Kendall*, 2010; *Hammond and Kendall*, 2016] and apply them to a field example of a migmatitic shear zone. This approach incorporates the CPO, chemistry, melt shape, and melt body orientation with respect to the seismic wave propagation direction, in order to evaluate expected uncertainties and possible signatures of the combined effect of these parameters on seismic velocities and anisotropies. Electron backscatter diffraction (EBSD) is used to measure CPO in the sheared migmatites, from which models invoking varying amount, shape and distribution of melt allow us to assess their impact on seismic properties. We explain how the models are built and work for a simple case, we then apply the modeling to geological and geophysical observations. We show that the interaction of all the modeled geological parameters play a key role in the seismic wave behavior which, as a consequence, behaves nonlinearly across the examined midcrustal shear zone analogue.

2. Seismic Modeling

We have developed four melt models that incorporate shape and crystal fabrics to model the seismic properties of mid to lower crustal melt (Figure 1): (a) "no fabric," (b) "shape fabric," (c) "layered fabric," and (d) "crystal fabric." Our starting point for the creation of models of seismic properties for partially molten rocks is to acquire EBSD data to give the mineral phase proportions as well as the CPO. The CPO and, consequently, its effect on seismic properties can be both strengthened or reduced during shear induced melting or anatexis, depending on the starting lithology and fabrics, associated phase reactions, and deformation style and magnitude. The inclusion of CPO into the models emphasizes the importance of the mineral composition and crystal fabric that can be up scaled to infer the seismic-scale crustal fabric, which in turns controls the seismic behavior [*Lloyd et al.*, 2011a]. Our modeling approach builds on previous studies modeling
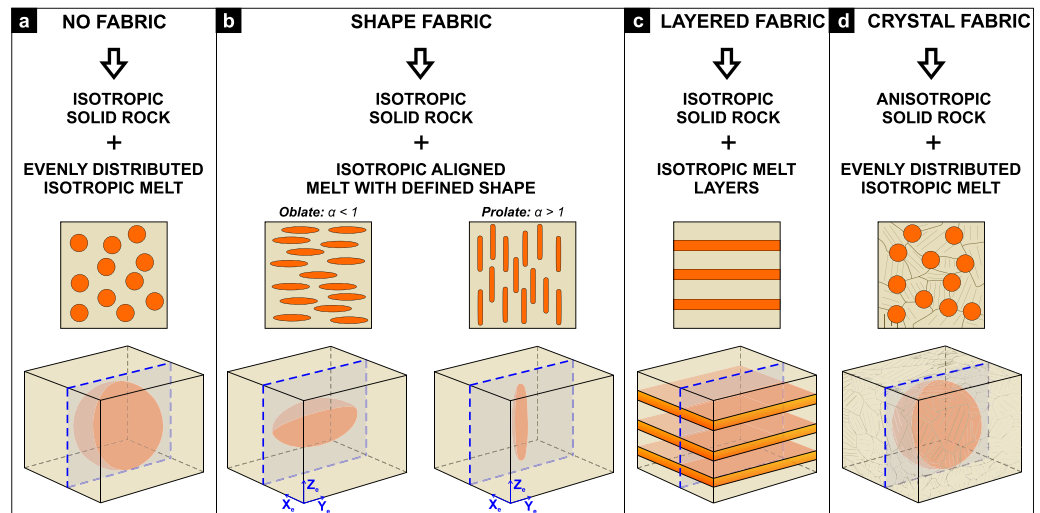
Figure 1. Melting models to calculate the seismic properties with variation in melt fraction: (a) no fabric, (b) shape fabric (based on *Tandon and Weng* [1984], adaptation of *Eshelby* [1957]), melt shape varies between oblate ellipsoids, $\alpha < 1$ (e.g., $\alpha = 0.1$ when X_e:Y_e:Z_e = 10:10:1), and prolate ellipsoids, $\alpha > 1$ (e.g., $\alpha = 10$ when X_e:Y_e:Z_e = 1:1:10), (c) layered fabric (based on the theory of *Backus* [1962]), and (d) crystal fabric models.

the effect of melt shapes, distributions and orientations on seismic properties on one hand [e.g., *Watanabe*, 1993; *Hammond and Humphreys*, 2000a; *Taylor and Singh*, 2002; *Hammond and Kendall*, 2016], and the CPO-based modeling method of *Mainprice and Humbert* [1994] and *Lloyd et al.* [2011a] on the other hand. Our approach aims to examine the combined effect of the key parameters which affect seismic behavior: melt body shapes and orientations, and the CPO of the solid phase.

The elasticity of the solid phase is based on CPO determined via EBSD at the University of Leeds. This system uses an FEI Quanta 650 scanning electron microscope (SEM) equipped with AZtec software and an Oxford/HKL Nordlys S EBSD system. The seismic properties of the constituent minerals and hence the bulk rock were predicted from the CPO according to the modal composition [*Mainprice and Humbert*, 1994]. The model methodology, therefore, takes into account the anisotropy induced by the measured mineral properties in the solid phase [*Lloyd et al.*, 2009]. We take this relatively standard approach further by then assigning melt fractions into the model in order to study how the combination of CPO-induced anisotropy and melt affects the seismic properties. Any melt fraction can be specified in the models, allowing the calculation of the seismic properties of the resulting rock-melt aggregate. In this approach, we have simply "melted" felsic minerals first without considering metamorphic phase reactions as the melting "progresses" (e.g., phase reactions from biotite or hornblende to pyroxene).

For the melt phase, we assume isotropic elasticity with a small but finite shear modulus. We assume a bulk modulus, K, of 16.1 GPa, appropriate for an andesitic composition [*Rivers and Carmichael*, 1987; *Bass*, 1995] and set the shear modulus, μ, of 0.01 GPa. For reference, $K = 13.5$ and 19.4 GPa for rhyolitic and basaltic melts, respectively [*Rivers and Carmichael*, 1987; *Bass*, 1995].These values give isotropic properties to the elasticity and to allow calculation of the Reuss bound a shear modulus > 0 GPa is applied [*Kushiro*, 1976; *Karato*, 2012]. The same elastic stiffness matrix is used for all melt phases. However, the density of melt varies according to melt composition [*Bottinga and Weill*, 1970], which is calculated via the "Magma-Density" spreadsheet [*Preston*, 2006]. A melt density is calculated for each "melted" mineral using the molar weight percent of oxides, wt %, molecular weight, M_W, giving the mole fraction, M_F (equation (1)), and molar volume at 800°C, M_T (the peak temperature for leucosome-rich domains in the natural example considered later) [*Menegon et al.*, 2011], from which a melt density, ρ, is calculated (equation (2)). Individual mineral melt densities are averaged according to modal proportion to give the whole melt composition assuming the same mixing laws as for solids.

$$M_F = \frac{\text{wt \%}/M_W}{\sum \text{wt \%}/M_W}, \tag{1}$$

$$\rho = \frac{\sum M_F / M_T}{\sum M_F / M_W}. \qquad (2)$$

The first and simplest model developed is the "no fabric model" (Figure 1a), which constrains an isotropic end member case. It uses an isotropic solid rock aggregate with isotropic melt evenly distributed as spheres, such that there is no shape or fabric effect for melt or for solid in this model. To calculate the isotropic elastic stiffness tensor, an upper bound Voigt aggregate tensor is calculated for the individual minerals in the sample using functions within the MTEX toolbox [*Bachmann et al.*, 2010; *Mainprice et al.*, 2015]. The Voigt average stiffness tensor of the solid rock aggregate, C, is given by averaging the elements of the rotated single crystal tensor giving the anisotropic elasticity [after *Walker et al.*, 2011]:

$$C_{ijkl}^V = \sum_{n=1}^N g_{i\alpha}^n g_{j\beta}^n g_{k\gamma}^n g_{l\delta}^n c_{\alpha\beta\gamma\delta}, \qquad (3)$$

where Bunge Euler angles describing the orientation of each crystal are converted into a rotation matrix, $g(\varphi_1, \Phi, \varphi_2)$, limits of summation (1 and N) bound the number of EBSD points and each point is assumed to represent an equal volume of sample. Repeated indices imply summation. Similarly, the Reuss average compliance tensor, S, is found using equation (4):

$$S_{ijkl}^R = \sum_1^N g_{i\alpha}^n g_{j\beta}^n g_{k\gamma}^n g_{l\delta}^n s_{\alpha\beta\gamma\delta}. \qquad (4)$$

The elastic stiffness tensor of the aggregate is calculated by Voigt-Reuss-Hill averaging of the single crystal elastic stiffness tensor, C, and compliance tensor, $S = C^{-1}$. The elastic properties of each mineral are calculated using the single crystal elastic stiffness matrix with no summation (c_{ij}, see Appendix A).

$$C_{ijkl}^H = \frac{C_{ijkl}^V + [S_{ijkl}^R]^{-1}}{2}. \qquad (5)$$

Individual Voigt tensors are compiled into an aggregate Voigt tensor according to the modal fraction of each mineral, alongside calculation of an aggregate density of the solid rock [*Anderson*, 1989]. A separate elastic stiffness tensor for melt is defined with a new melt density [*Preston*, 2006]. The bulk and shear moduli are defined for the solid and melt fractions and when combined, these return an isotropic elasticity matrix for the aggregate and the melt. The solid rock matrix is then combined with the melt matrix and converted to a Voigt tensor (equation (6)). Aggregate elastic stiffness tensors (C) and densities (ρ) for solid rock and melt fractions are calculated using the following equations within the no fabric model:

$$C = C_{agg}(1-\phi) + C_{melt}\phi, \qquad (6)$$

$$\rho = (\rho_{agg}(1-\phi) + \rho_{melt}\phi), \qquad (7)$$

where C_{agg} is the solid rock aggregate elasticity tensor, C_{melt} is the isotropic melt elasticity tensor, ϕ is the melt fraction, ρ_{agg} is the solid rock density, and ρ_{melt} is the isotropic melt density.

A development of the no fabric model is the shape fabric model (Figure 1b). This model uses effective medium theory to build analytical models of the macroscopic properties of composite materials. *Tandon and Weng* [1984] adapted *Eshelby* [1957] inclusion theory for an isotropic inclusion in an isotropic matrix. *Eshelby* [1957] developed analytical solutions to calculate strain of ellipsoidal inclusions in an isotropic matrix. The shape fabric model incorporates a shape variant for the aligned melt inclusions within the isotropic rock aggregate, applied using the MSAT toolbox [*Walker and Wookey*, 2012]. Melt shape is modeled with a defined aspect ratio (α). For oblate ellipsoids $\alpha < 1$ (e.g., $\alpha = 0.1$ when $X_e:Y_e:Z_e = 10:10:1$), and are used to represent isolated melt pockets, sheets and pillows. Spheres have an $\alpha = 1$ ($X_e:Y_e:Z_e = 1:1:1$) and produce an identical model to the no fabric model. Prolate ellipsoids, $\alpha > 1$ (e.g., $\alpha = 10$ when $X_e:Y_e:Z_e = 1:1:10$),

represent elongate magma tubes or tunnels as well as smaller pockets. Here α is modeled between 10^{-4} and 10^4, with a value of 10^{-2} used as an analogue for crustal melt layers or lenses as this is the minimum aspect ratio estimated from the field example (see section 4).

The layered fabric model (Figure 1c) also builds on functions within the MSAT toolbox, but this time applying the theory of *Backus* [1962] via an effective medium framework. Backus theory assumes that when isotropic layering is finer than the seismic wavelength, it can be replaced by a homogeneous transversely isotropic medium that behaves identically to the actual medium under static load in the infinite wavelength limit. In this case, the model is built by thin horizontal layers of isotropic rock aggregate and isotropic melt, with melt volume assigned via varying the layer thickness.

In the aforementioned models, the solid aggregate is isotropic but in nature this is rarely the case. The crystal fabric model (Figure 1d) uses an anisotropic solid phase aggregate with a mineral CPO. The fabric is combined with an evenly distributed isotropic melt with the aspect ratio of a sphere. The solid phase fabric is, therefore, taken into consideration here but melt shape is not modeled. The upper bound Voigt aggregate tensor is calculated from the mineral CPO and the elastic stiffness tensors and individual densities for both the solid rock and melt are combined in accordance with the modal and melt fractions (equations (6) and (7)).

Once the density and elasticity of the melt-rock aggregate has been established, the next step is to find the velocities of seismic waves passing through each model. As these models are anisotropic the phase velocities vary with propagation direction and for any general direction three elastodynamic plane waves can be supported: a fast quasi-compressional wave, qP, with particle motion close to the wave propagation direction, and two quasi-shear waves, qS1 and qS2, with different velocities and mutually orthogonal particle motion normal to that of qP. As most of our models exhibit hexagonal symmetry, we drop the quasi- prefix and name these phases P, S1, and S2, and their phase velocities Vp, Vs1, and Vs2, respectively (Vp $>$ Vs1 $\geq$ Vs2). For a given propagation direction, these velocities are found from the three eigenvalues, λ_1, λ_2, and λ_3 of the of the Christoffel tensor, **G** $G_{ik} = C_{ijkl} n_j n_l$, where **n** is the unit vector pointing in the propagation direction. Once the eigenvalues are sorted the phase velocities are given by

$$Vp = \sqrt{\frac{\lambda_1}{\rho}}, Vs1 = \sqrt{\frac{\lambda_2}{\rho}}, Vs2 = \sqrt{\frac{\lambda_3}{\rho}}. \qquad (8)$$

The eigenvectors of **G** give the particle motion directions for the three phases. In practice, we either evaluate the three phase velocities for a propagation direction accessible to seismological observation or calculate the phase velocities on a grid of directions to allow contouring the phase velocity surfaces as stereographic projections. The calculations and plotting make use of the MTEX toolbox [*Bachmann et al.*, 2010; *Mainprice et al.*, 2011]. We also calculate some derived seismic properties based from the phase velocities. In particular, we for each propagation direction we estimate the magnitude of shear wave splitting expressed as a percentage shear wave anisotropy, AVs, from

$$AVs = 200 \frac{Vs1 - Vs2}{Vs1 + Vs2}, \qquad (9)$$

and evaluate the ratio of *P* and *S* wave velocities (Vp/Vs1 and Vp/Vs2), which can be compared to receiver function analysis. However, it is important to note Vp/Vs measured in receiver functions is typically for the whole crust rather than a single solid-melt aggregate as shown in the results here. To estimate Vp/Vs for the whole crust rather than a single solid-melt aggregate, we isolate the time, *t*, from individual sample velocities, by using hypothetical depths and sum over crustal layers (equation (10)).

$$Vp/Vs = \frac{\Sigma t_s}{\Sigma t_p}. \qquad (10)$$

The final step is to relate the velocities calculated in an abstract model to a geographic reference frame that can be related to the Earth. The modeling and sample reference frame, $X_m:Y_m:Z_m$, relates to the orientation of the symmetry axis. In the case of an oblate melt inclusion, the symmetry axis is in the Z_m direction.
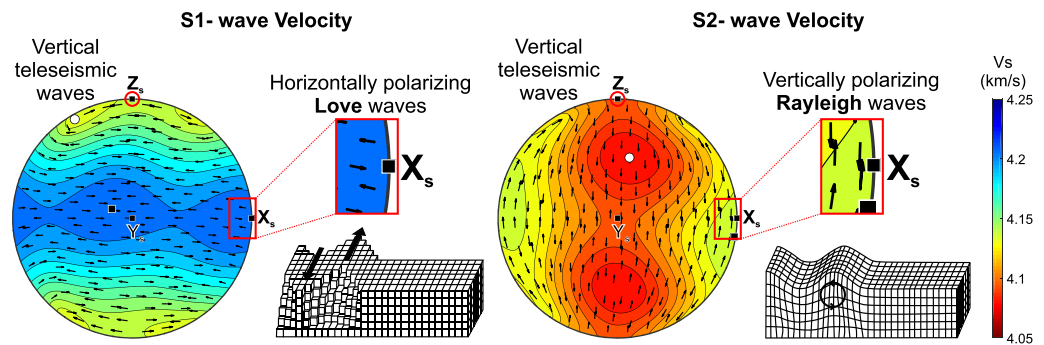
Figure 2. Example stereographic projections of Vs1 and Vs2 indicating where analogue teleseismic and surface wave data are taken from. Surface wave data are taken from the X_s–Y_s plane and teleseismic data are taken from X_s. The Vs1 plot shows horizontal polarization representing Love waves, whereas Vs2 polarizes vertically and represents Rayleigh waves.

Samples are analyzed via EBSD in the kinematic reference frame where the X_m–Y_m plane is parallel to the foliation plane and X_m is parallel to the stretching lineation.

Seismic waves propagate in a geographic reference frame, X_s:Y_s:Z_s. Surface waves propagate horizontally and hence can be derived from the horizontal X_s–Y_s plane in the models. Love and Rayleigh waves are distinguished by the shear wave polarization direction (Figure 2). Love waves polarize horizontally and are typically faster (Vs1) than vertically polarizing Rayleigh waves (Vs2) in most models. In contrast, receiver functions and shear wave splitting come from teleseismic waves and assume a vertical path. Thus, they can be derived from the Z_s direction which is vertical in the models (Figure 2).

3. Model Results

In order to show the general behavior of each model, we have used sample SIP20 (see Table 1) considered cases from 0 to 40% melt, after which value the crystal framework for an effective medium breaks down and viscosity rapidly decreases [*Lejeune and Richet*, 1995; *Rosenberg and Handy*, 2005]. The seismic results for the four models (no fabric, shape fabric, layered fabric, and crystal fabric) are plotted in 3-D via stereographic projections for a 20% melt volume (Figure 3) and also as analogues for surface waves, X_m–Y_m, and teleseismic, Z_m (Figure 4). Unless stated the model reference frame (X_m:Y_m:Z_m) are equal to the geographic reference frame (X_s:Y_s:Z_s).

3.1. 3-D Seismic Projection

Stereographic projections of seismic properties for each model show the elastic stiffness relationship when 20% melt is introduced to the solid rock (Figure 3). As expected, the no fabric model has no variation in 3-D space, yielding identical values for the maximum and minimum in each seismic property, it is isotropic. The impact of the alignment of melt can clearly be recognized in the shape and layered fabric models. When the melt inclusion symmetry axis is parallel to Z_m (e.g., layered fabric model, horizontally aligned oblate ellipsoids and vertically aligned prolate ellipsoids in the shape fabric model) velocity lows are parallel to X_m and Y_m. This behavior switches if the melt inclusions are rotated and the symmetry axis is in the X_m direction, where velocity lows parallel to Y_m and Z_m. The stiffness matrices for the layered fabric model are similar to those for horizontal oblate ellipsoids in the shape fabric model melt, and hence produce similar seismic velocity behavior. The crystal fabric model considers the mineral CPO and results in a nonuniform seismic projection. This indicates that the CPO induces an anisotropy into the solid phase and, therefore, to the bulk solid-melt aggregate, however, the mineral CPO effect is weakened as melt volume increases. Variations in orientation within the shape fabric model simply alter the alignment of the symmetry axis, as the maximum and minimum are identical for each variation.

Large difference between Vs1 and Vs2 for oblate ellipsoids and layered melts produce large *S* wave anisotropies. Here we show the results for oblate ellipsoids with an α of 10^{-2}, the layered fabric model and oblate ellipsoids give similar results if $\alpha = 10^{-4}$ as this aspect ratio is large enough to be comparable with continuous ("infinite") layers. The large differences between Vs1 and Vs2 also result in large Vp/Vs ratios as Vs1 $\gg$ Vs2. For horizontal oblate ellipsoids in the shape fabric model, the Vp/Vs1 ratio is 60%
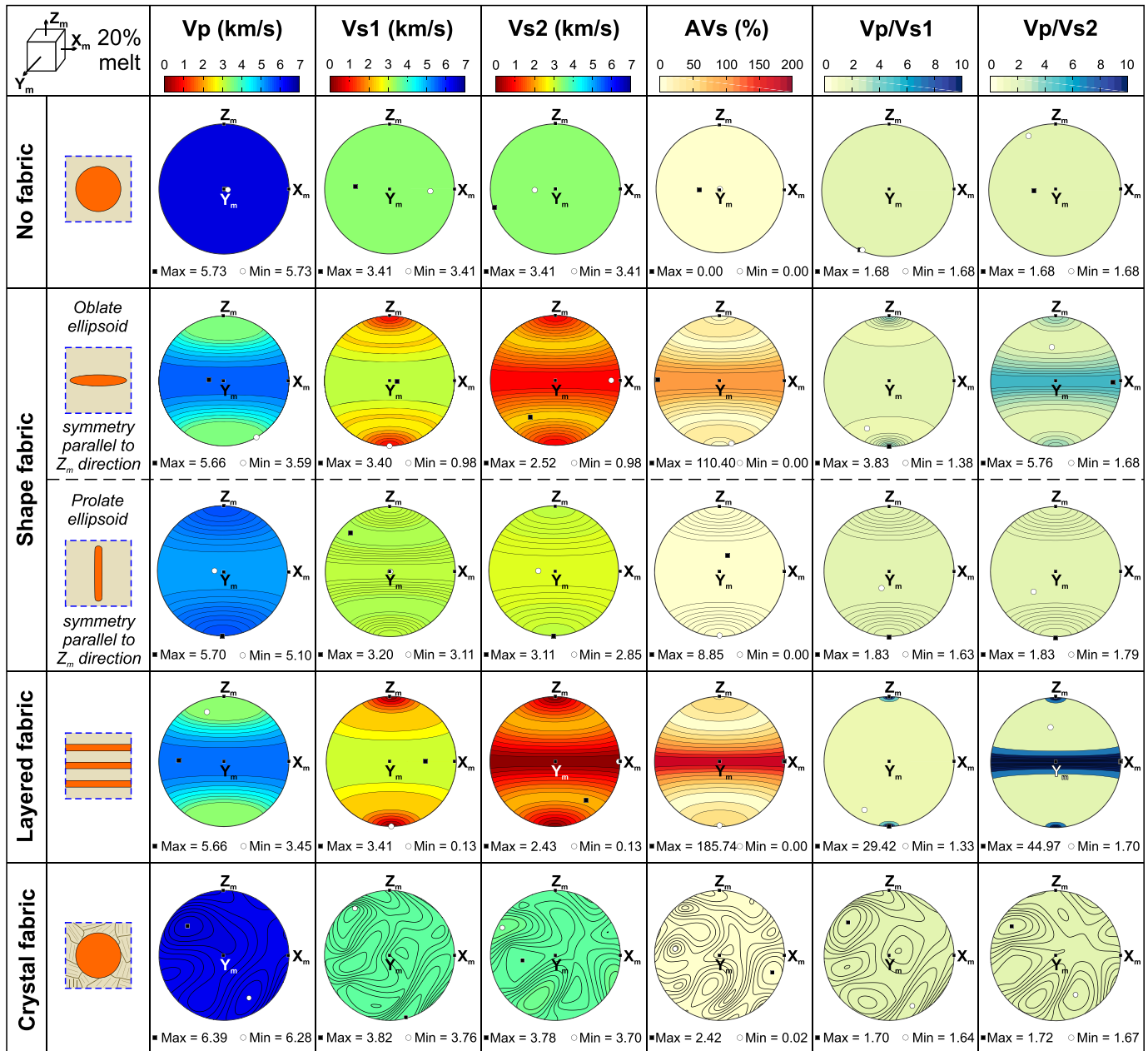
Figure 3. Antipodal stereographic projections of the seismic properties at 20% melt for each model. The projections show the relationship of the seismics in 3-D. Analogues to teleseismic data are taken from the vertical Z_m direction, surface wave data are taken from the horizontal X_m–Y_m plane. The symmetry axis for all models is in the Z_m direction. Common scales for Vp, Vs1 and Vs2, AVs and Vp/Vs for all models. Black squares and white circles indicate the maximum and minimum points, respectively.

lower than the Vp/Vs2 ratio. Similarly, Vp/Vs1 is also 60% lower than Vp/Vs2 for the layered fabric model, although the maximum ratio is much larger at 27.76 for Vp/Vs1 and 43.46 for Vp/Vs2. These very high Vp/Vs ratios are much larger than measured from the field (e.g., the Afar Rift in Ethiopia has a maximum Vp/Vs of 2.2) [*Hammond et al.*, 2011], this is the result of not measuring Vp/Vs over the whole crust and focusing on a solid-melt aggregate.

3.2. Surface Waves

Surface waves propagate in the X_m–Y_m plane and are sensitive to the *S* wave velocity. Where Vs polarizes horizontally the surface wave signal would represent Love waves, Vs1 polarizes horizontally for all models except prolate ellipsoids with a symmetry axis parallel to Z_m (Figures 2, 4, X–Y2). While Vs2 polarizes vertically and
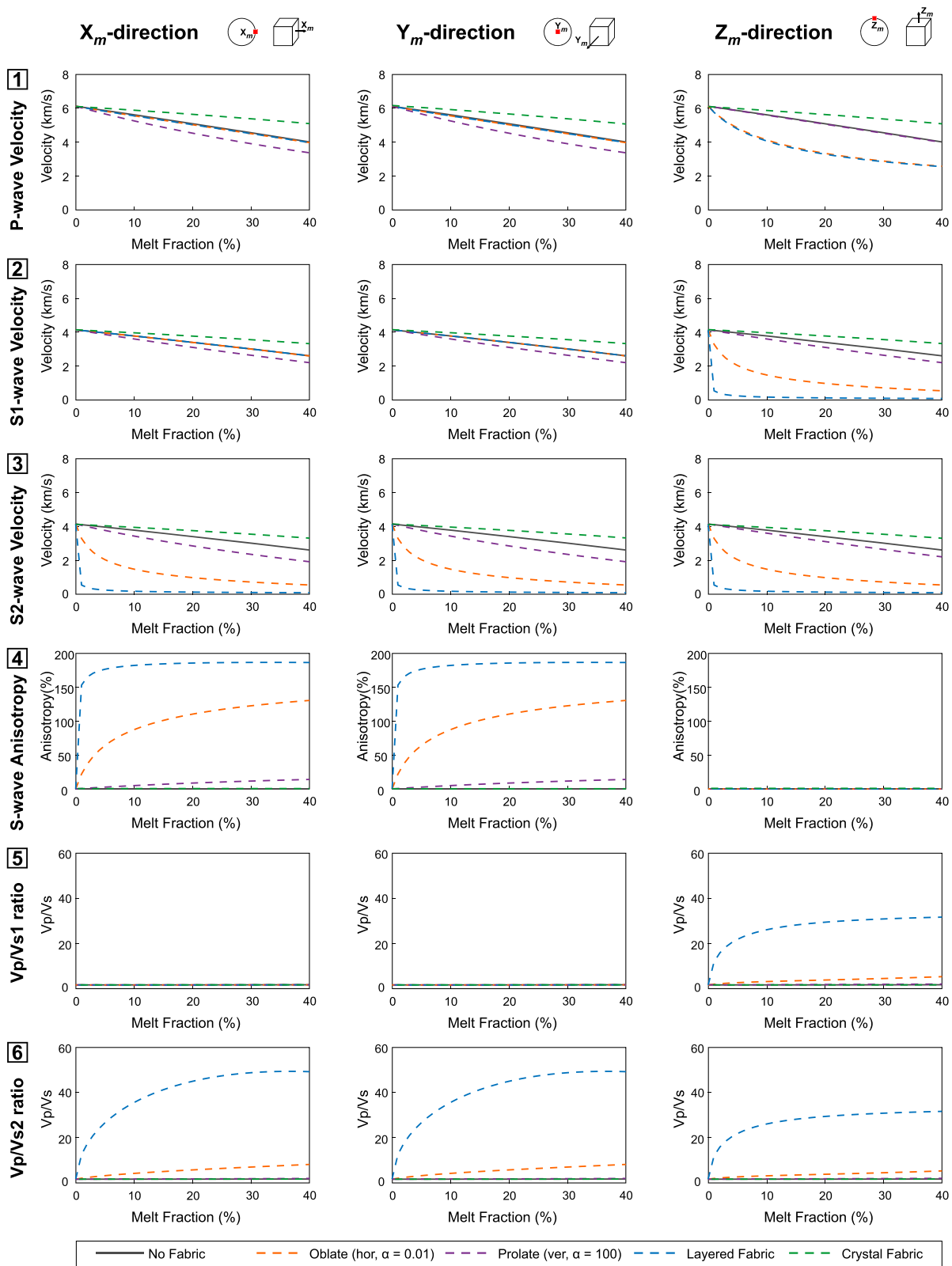
Figure 4. Seismic properties for each model with variations in the shape fabric model. Calculated seismic results (1–6) are shown for waves propagating in the X_m, Y_m, and Z_m directions. The aspect ratios used in the shape fabric are $\alpha = 10^{-2}$ for oblate ellipsoids and $\alpha = 10^2$ for prolate ellipsoids and the symmetry axis is in the Z_m direction.
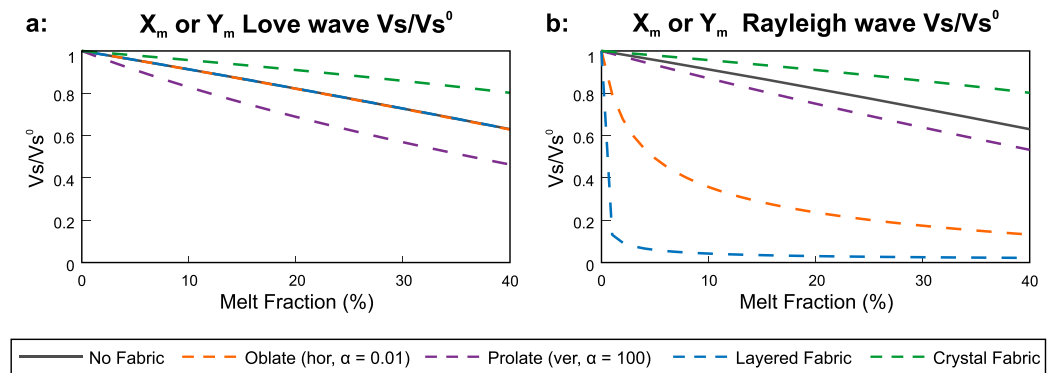
Figure 5. Shear wave velocity reduction (Vs/Vs^0) for each model for (a) Love and (b) Rayleigh waves from the X_m or Y_m directions.

represents Rayleigh waves (Figures 2 and 4, X–Y3). The no fabric, crystal fabric and prolate ellipsoids in the shape fabric models give a linear decrease for both Love (Vs1) and Rayleigh (Vs2) waves, decreasing at different rates between models. In the X_m direction for Love waves for the layered fabric and the horizontal oblate ellipsoids in the shape fabric models, the decrease is also linear but variable between models (Figure 4, X2). Whereas it is nonlinear for Rayleigh waves for the same models, with a rapid decrease in velocity to 25% melt, followed by a more gradual decrease to near 0 km/s at 40% melt (Figure 4, X3). A similar behavior is observed in the Y_m direction for these models (Figure 4, Y2–3). Strong variations between Love and Rayleigh wave velocities have been observed in melt-rich volcanic settings. For example, Love waves propagate faster than Rayleigh waves in a magmatic sill complex beneath the Toba caldera [*Jaxybulatov et al.*, 2014] and a strong radial anisotropy observed in the crust beneath Costa Rica is attributed to the presence of melt-rich sills [*Harmon and Rychert*, 2015].

The variations in Vs are reflected in the AVs behavior (Figure 4, X–Y4): AVs is 0% where there is no difference between Love and Rayleigh waves, but equally very large anisotropies are induced when there are differences between Love and Rayleigh waves. The greatest AVs observed is for the layered fabric model, where AVs increases rapidly to ∼180%. This same behavior but increasing up to ∼120% is seen for horizontal oblate ellipsoids in the X_m and Y_m directions. Prolate ellipsoids also show an AVs increase up to 20% at 40% melt in the X_m and Y_m directions. The crystal fabric model has a constant AVs between 0 and 4% depending on initial mineralogy of the sample. *Hammond and Kendall* [2016] also modeled the effect of oblate to prolate ellipsoidal shaped melt on seismic properties for the Afar Rift, Ethiopia, they found similar results for a large radial anisotropy when oblate ellipsoids are modeled.

Figure 5 shows the results for the reduction of surface wave velocities where Vs/Vs^0 is the Vs at the specified melt fraction divided by the Vs^0 at 0% melt. Love and Rayleigh waves are calculated for the X_m and Y_m directions. All models show a reduction of Vs/Vs^0, but this reduction is not linear for models which include low aspect ratio melt inclusions. For Love waves, Vs/Vs^0 decreases linearly for the no fabric and layered models and horizontal oblate ellipsoids in the shape fabric model. The crystal fabric model also decreases linearly but at a slower rate, whereas vertical prolate ellipsoids decrease faster. For Rayleigh waves, Vs/Vs^0 behaves identically to Love waves for the no fabric and crystal fabric models as well as horizontal prolate ellipsoids in the shape fabric model. Prolate ellipsoids show a slower rate of decrease for Rayleigh wave reduction than they did for Love wave reduction. Oblate ellipsoids show a rapid decrease in Vs/Vs^0 and the layered fabric exhibits an even faster reduction. The symmetry axis of all the models is orientated in the Z_m direction, thus surface waves for the X_m:Y_m plane is nondirection dependent.

3.3. Teleseismic Waves

Seismic waves travelling in the Z_m direction (approximate analogue for subvertical teleseismic waves) are shown in Figure 4 (Z1−6). For most models, Vp shows a linear decrease but at differing rates depending on the model, with the layered fabric and the horizontally orientated oblate ellipsoids in the shape fabric model showing an initial rapid decrease before decreasing at a slower rate after ∼25% melt is introduced (Figure

4, Z1). Vs decreases linearly for most models (Figure 4, B–C3), however, the layered fabric and oblate ellipsoid models show initial nonlinear behavior.

AVs can be measured from teleseismics via shear wave splitting where the shear wave window limits the use of Vs to within 35° of vertical, here we calculate the AVs to illustrate the model properties. A 0% anisotropy is observed for the no fabric, shape fabric and layered fabric models (Figure 4, Z4). Vs1 and Vs2 are equal in the Z_m direction for these models as the symmetry axis is also orientated in the Z_m direction. The crystal fabric model has a constant AVs of 1.67% due to small variations in Vs caused by the solid rock anisotropy.

Vp/Vs can be measured via receiver functions, back azimuthal variations can be used to acquire two Vp/Vs values [*Hammond*, 2014]. Here Vp/Vs is 1.66 at 0% melt for all models increasing to 1.73 at 40% melt for the no fabric and crystal fabric models and 2.03 at 40% melt for prolate ellipsoids in the shape fabric model. Oblate ellipsoids exhibit a faster rate of increase in Vp/Vs1 and Vp/Vs2 increasing up to 5.32 at 40% melt (Figure 4, Z5–6). The layered fabric model increases rapidly and nonlinearly to Vp/Vs of ∼30 where it remains approximately constant after ∼15% melt.

Regional tomography is sensitive to Vp in near vertically propagating waves approximately in the Z_m direction. One way to recover Vp in the X_m–Y_m plane could be refraction tomography (e.g., Pn tomography), which, if the refracting interface is above the melt zone, could reveal azimuthal variation in the horizontal *P* wave velocity in the melt layer [*Hammond and Kendall*, 2016]. Vp shows similar behavior for most models, with a linear decrease for increasing melt fraction (Figure 4, X–Y1). Even in the case of linear decrease, it is not identical for all models: the crystal fabric model decreases in Vp at a slower rate than the no fabric and layered fabric models, whereas prolate ellipsoids in the shape fabric model decrease at a faster rate.

For the Vp/Vs1 in the X_m and Y_m directions, all models show low ratios (1.66 at 0% melt to 1.71–1.73 at 40% melt), reflecting the Vp and Vs1 behaviors described above (Figure 4, X–Y5). This relationship is also observed in the X_m and Y_m directions for Vp/Vs2 for the no fabric, prolate ellipsoids, and crystal fabric model. Vp/Vs2 for oblate ellipsoids shows a gradual increase up to 8.18 at 40% melt and reaches ∼50 for the layered fabric model. *Hammond and Kendall* [2016] also calculated a high Vp/Vs ratio from receiver functions and vertically polarizing Vp/Vs when an oblate ellipsoidal melt inclusion is modeled.

3.4. Rotation of Melt Inclusions
An oblate ellipsoid can be used as an application for isolated melt pockets and sheets with finite dimensions (at the scale of the seismic wavelet) and low aspect ratios, reflecting an overall flattening of the rock volume during melting (e.g., lenses of melt parallel to foliation in orogenies). Melt shaped like prolate ellipsoids can be used as an analogue for elongate magma tubes or smaller melt pockets with finite dimensions and high aspect ratios where the rock is subjected to overall constriction during melting (e.g., magma tubes to transport melt in low strain regions). In both cases, the melt volumes often, although not always, follow pre-existing geological features such as bedding, foliation, or shear zone/fault planes. These geological features are usually not at perfectly right angles to the seismic wave propagation direction, whereas the models above and those often used in literature presume this to be the case. However, the angle of incidence of the seismic wave with respect to the feature being imaged greatly affects the observed seismic signal.

Figure 6 illustrates the results for each seismic property at 20% melt when the ellipsoids are rotated with respect to the wave propagation direction. As the symmetry axis for oblate melt inclusions is in the Z_m direction, therefore rotations of 90° are shown around the X_e or Y_e planes and measured from Z_m. The symmetry axis for vertically orientated prolate ellipsoidal shaped melt inclusions is also in the Z_m direction and seismic properties are measured from this direction when rotated around the X_e or Y_e planes. Below each graph is a stereographic projection at 15° intervals of the Vp, Vs1 and Vs2 to show how they change as the inclusions are rotated. For oblate ellipsoids, there is a large variation in seismic velocity as the inclusions are rotated. The velocity changes are not linear as shown by the velocity and Vp/Vs ratio graphs. Where Vs1 and Vs2 are equal there is no shear wave splitting, and hence no anisotropy is observed at 0° and the inflection point at 45°. For prolate ellipsoids, velocity change with rotation is not as pronounced. Variation between Vs1 and Vs2 between 60° and 90° induces a 10% anisotropy and the Vp reduces only slightly between ∼20° and 60° rotation.
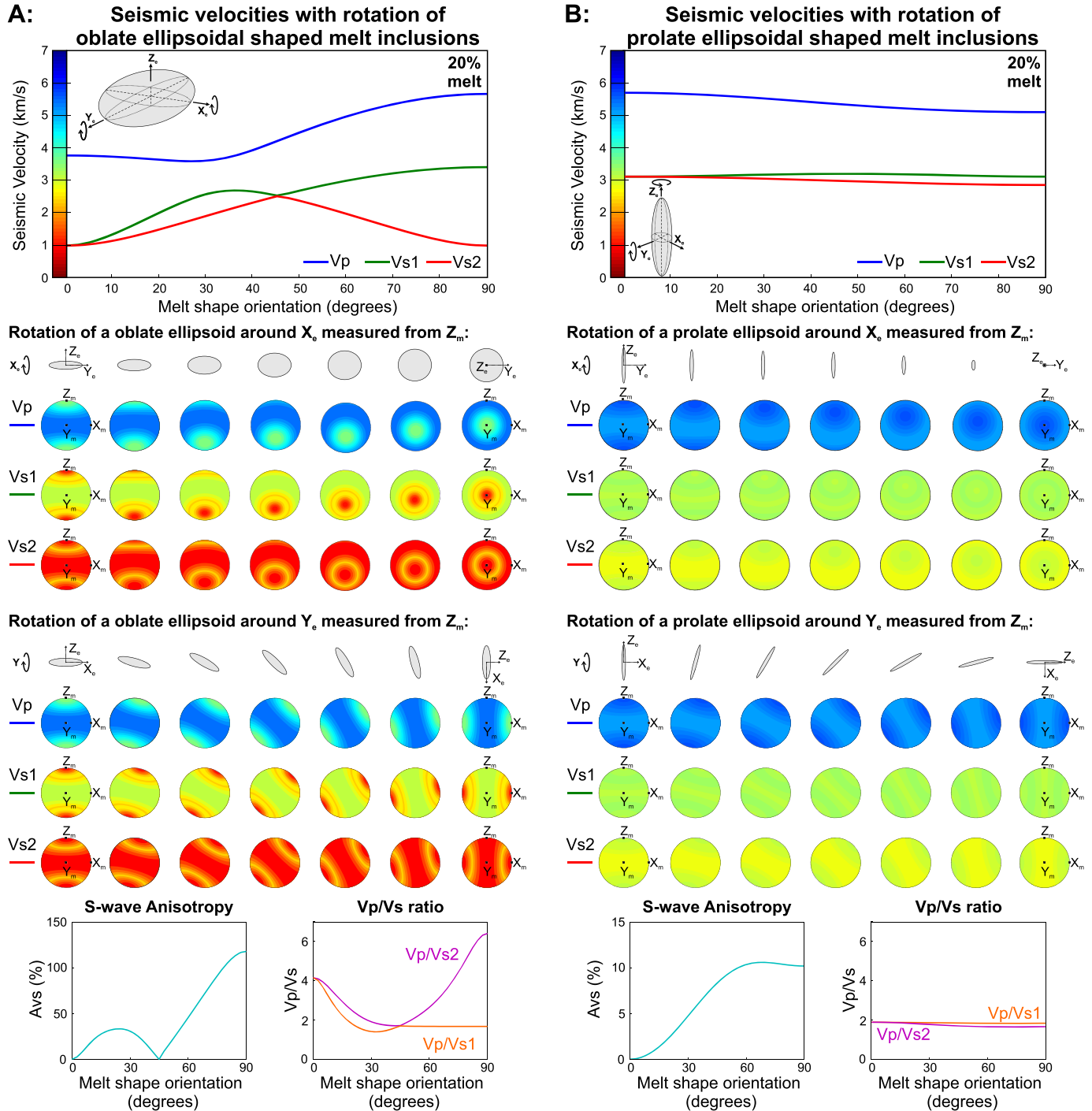
Figure 6. Change in Vp, Vs1, and Vs2 with rotation of melt inclusions at 20% melt volume. (a) Rotation of oblate melt inclusions ($\alpha = 10^{-2}$) around the X_e or Y_e, measured from the Z_m direction; (b) rotation of prolate melt inclusions ($\alpha = 10^2$) around the X_e or Y_e axis, measured from the Z_m direction. AVs and Vp/Vs relationship with melt inclusion orientation is shown and seismic stereographic projections of Vp, Vs1, and Vs2 for the rotated melt inclusions are shown beneath the graphs.

4. Application to Migmatites

To test the models in a geological setting, we take a simple system to explore the range of results before finally comparing with results from an active orogen. Our melting models are applied to samples collected across a migmatized shear zone, in order to investigate how the observed changes in melt fraction, melt
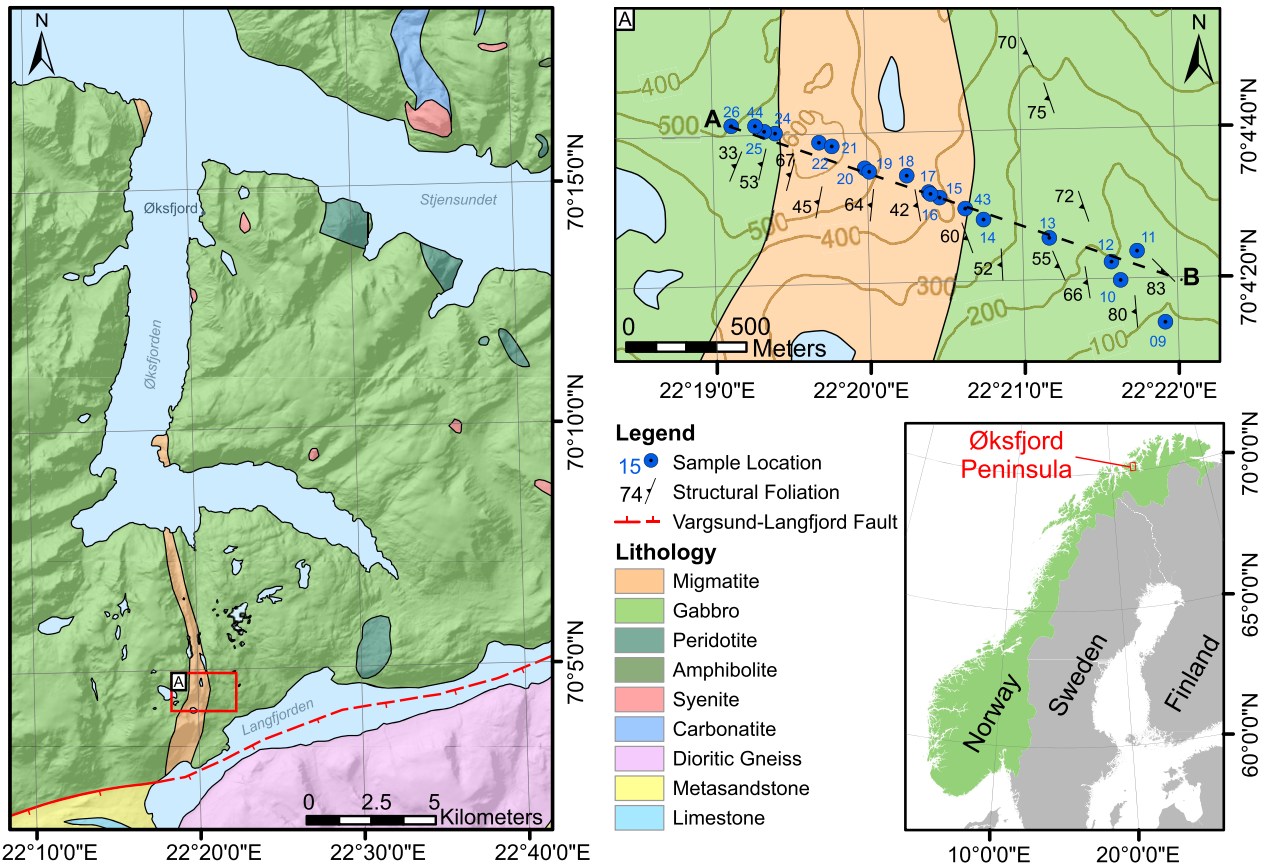
Figure 7. Geological map showing key lithologies of the Øksfjord peninsula in the southern Seiland Igneous Province (modified from *Roberts* [1973]). Detailed map A shows a traverse through a migmatitic shear zone with sample locations identified in blue, section line X–X′ corresponds to the graphs in Figure 9.

pocket/layer shape and orientation, and the CPO of the solid phase affect the seismic wave behavior across a deep crustal, partially molten layer. The field example, therefore, serves as an analogue for a deep crustal partially molten shear zone/layer such as has been assumed to exist under the Himalayan-Tibetan crust. The results underline the difficulty of interpreting melt fractions from seismic data.

The field analogue comes from the Seiland Igneous Province (SIP), western Finnmark, Northern Norway (Figure 7). The SIP forms the uppermost structural unit of the Kalak Nappe Complex [*Sturt et al.*, 1978]. It consists of a suite of deep-seated magmatic rocks ranging in composition from ultrabasic to nepheline syenitic and carbonatitic [*Krogh and Elvevold*, 1990; *Elvevold et al.*, 1994]. The intrusive event was short lived between 579 and 550 Ma and emplaced during a preorogenic extensional phase related to the initial stages of the opening of the Iapetus Ocean [*Roberts et al.*, 2006]. The magmatism was much more voluminous than the current surface exposure of 5400 km^2, which only represents the roots of the intrusions [*Roberts et al.*, 2006]. The oldest rocks in the Øksfjord area are garnet-bearing paragneisses from the Eidvågeid Sequence [*Akselsen*, 1982]. The plutons have intruded these paragneisses of unknown age, and resulted in at least one phase of partial melting of the gneisses [*Krogh and Elvevold*, 1990]. The resulting peak-temperature granulite facies mineral assemblage includes a quartzofeldspathic leucosome with often abundant garnet porphyroblasts. The sampled traverse is across an intensely deformed, migmatized paragneiss shear zone sandwiched between two mafic plutons (Figure 7). Samples are cut in the kinematic reference frame where X_m is parallel to the mineral stretching lineation and X_m–Y_m is parallel to the foliation plane. Samples are mounted exposing the X_m–Z_m plane, the profile plane to the shear zone for that sample; although this plane is sample dependent its orientation is approximately 020/40E.

Figure 8. Representative field photographs of the migmatized paragneiss in the SIP. (a) Melt localizes and forms bands around garnet porphyroblasts. (b) Small-scale stromatic banding between leucosome and restite; leucosome consists of felsic bands of quartz, plagioclase, k-feldspar, and garnet, with mafic minerals forming the restite portion of the rock. (c) Folding of the stromatic bands in the migmatite; leucosome and restite are clearly visible in this outcrop.

The paragneisses display mainly stromatic migmatites although some ptygmatic or schollen structures also occur [see e.g., *Wimmenauer and Bryhni*, 2007, for migmatite terminology and classification]. Stromatic migmatites are observed on a variety of scales (Figure 8). The stromatic layering of the migmatite shows the segregation of the leucosome (felsic) and melanosome (mafic) neosome stroma of various thicknesses from 1 to 500 mm. The center of the migmatized area mainly shows linear stroma but, in some places tight parasitic folds deform the stromatic migmatite. For most folded migmatites layer thickness remains constant (Figure 8c), but in some localities the leucosome varies in thickness and the fold hinges in the restite thicken forming similar folds. The edges of the paragneiss zone sometimes display schollen structures where rafts of nonmigmatized restite remain intact and the leucosome flows around the rafts. More distally, where the rock is predominantly gabbroic, there are occasional migmatite flow channels. These channels increase in frequency toward the paragneiss and eventually blend into the paragneiss and indicate a graduated contact between the paragneiss and the gabbro.

Seismic properties were calculated for multiple samples from a traverse across a shear zone in the SIP for the four models: no fabric, shape fabric, layered fabric, and crystal fabric. The paleomelt fraction varies for each sample and has been quantified by microstructural analysis of the sample—optical analysis of mineralogical grain textures and study of Euler angles for individual phases (see Table 1 for detail on melt quantification). Results shown in Figure 9 are for waves propagating in the horizontal X_m and Y_m directions and vertical Z_m direction, giving analogues to surface and teleseismic waves respectively at the time of melting. These models, therefore, assume the melt pockets are either vertical or horizontal in the crust, in order to provide a simplified example of the effect of the different melt configurations alone. It should be noted that additional complexity, as shown in Figure 6, would result from the equally realistic case of an anatectic layer that is inclined (i.e., at an angle to the seismic wave propagation direction).

All models show the expected general trend of a velocity reduction with increasing melt fraction but it is not a simple linear trend and there are significant differences between models. Mineral properties (matrix density and elastic stiffness) and CPO strength have a significant effect on the seismic velocities, although the latter is only present for the crystal fabric model. For example, the strongly orientated minerals in sample SIP43 (Table 1) cause a greater increase in the velocity for this sample compared to others at the same melt fraction of 15%. The layered fabric model therefore shows a much larger reduction of Vs2 compared to the other models (Figure 9, Z1–3), and the oblate vertical model shows consistently lower Vp and Vs than most other models (Figure 9, XYZ–1).

When Vs1 and Vs2 are equal, AVs is zero, as shown for the no fabric, shape fabric (when melt is horizontal) and the layered fabric models (Figure 9, XYZ–4). The vertical oblate ellipsoids in the shape fabric model show an increase of AVs of up to 120% with greater melt volumes compared to 12% for vertical prolate ellipsoids. This is due to the isotropic melt shape component inducing strong anisotropy. The small differences between Vs1 and Vs2 in the crystal fabric model yields a decreasing AVs with increased melt, but the AVs variation is minimal when compared with the large increase in AVs caused by the vertical inclusions in the shape fabric model.
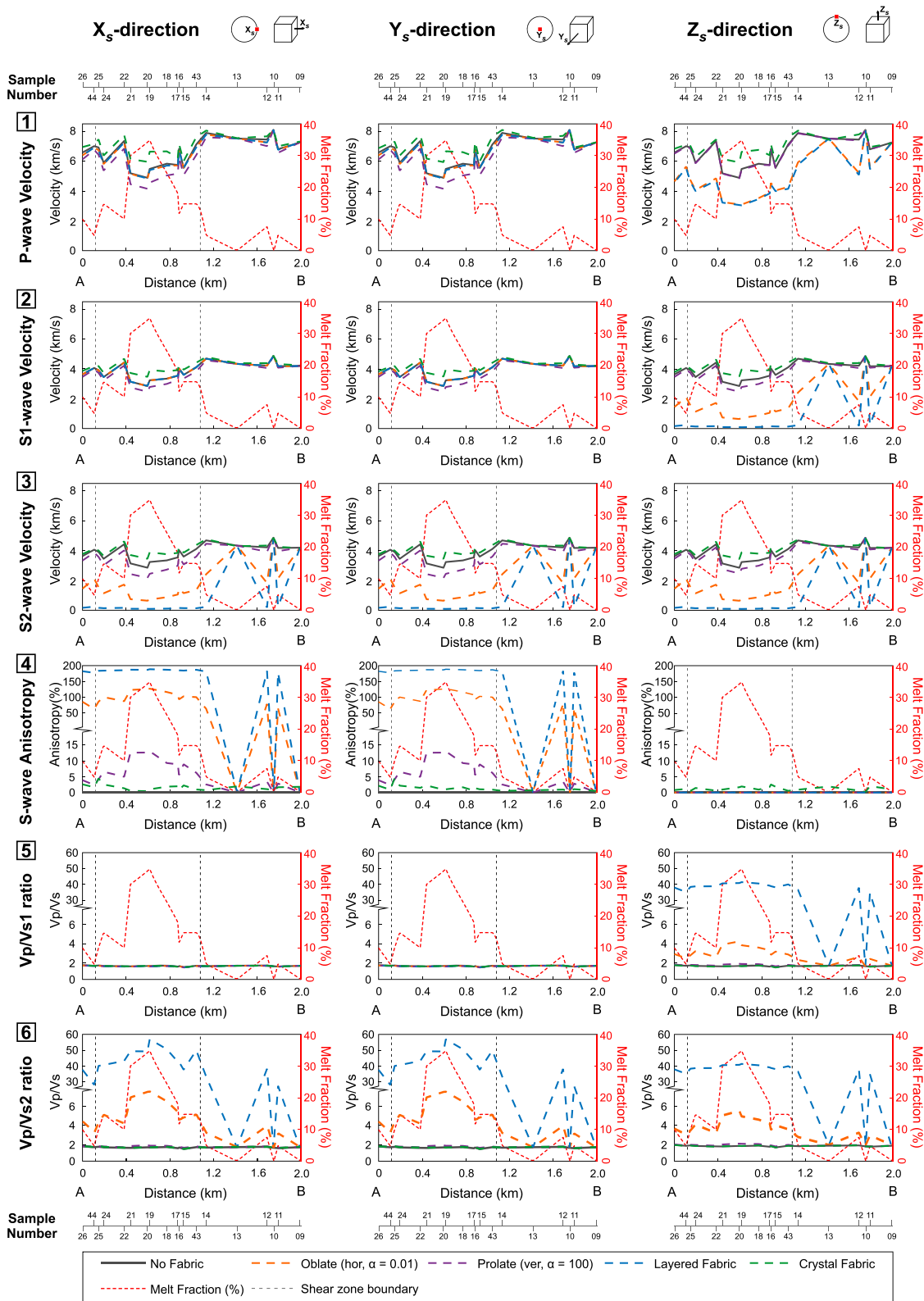
Figure 9. Change in seismic properties across the migmatitic shear zone for each of the four models with additional variation in the shape fabric model. Seismic property results (1–6) are shown for waves propagating in the X$_m$, Y$_m$, and Z$_m$ directions (Figures 3 and 4). Note y axis scale change in 4–6. Relative sample location along the section line is shown in the bottom left diagram. Melt fraction calculated from field and microstructural studies and indicated by the orange dashed line.

Table 1. Rock, Mineral, and Melt Properties of Samples Used in the a Melt Layer Seismic Study[a]

| | | | | Melt Volume Determination Technique | |
Sample Number	Lithology	Mineralogy	Melt Fraction	Field	Microstructures
SIP09	Gabbro	Pl, Opx, Ilm, Bt	0	No foliation, leucosome not present.	Subhedral to euhedral crystals, low dihedral angles.
SIP10	Gabbro	Opx, Pl, Ilm	0	No foliation, leucosome not present.	Equigranular, euhedral crystals.
SIP11	Migmatite	Qz, Kfs, Alm, Pl, Ilm, Bt	5	Segregation of leucosme and melanosome, stromatic-type migmatite.	Recrystallization of Qz and Pl.
SIP12	Migmatite	Kfs, Alm, Qz, Pl, Ilm	8	Segregation of leucosme and melanosome, stromatic-type migmatite.	Recrystallization of Kfs and Pl.
SIP13	Gabbro	Cpx, Pl, Ilm	0	Foliated but leucosome not distinct.	Subhedral to euhedral crystals, low dihedral angles.
SIP14	Gabbro	Opx, Pl, Ilm, Hbl	5	Foliated with leucratic portions.	Equigranular, subhedral crystals.
SIP15	Migmatite	Qz, Kfs, Opx, Pl, Bt, Alm	15	Segregation of leucosme and melanosome, stromatic-type migmatite.	Recrystallization of Qz and Pl.
SIP16	Migmatite	Opx, Pl, Kfs, Qz, Ilm	12	Segregation of leucosme and melanosome, schollen-type migmatite.	Recrystallization of Pl, Kfs, and Qz.
SIP17	Migmatite	Qz, Kfs, Alm, Pl, Bt	18	Segregation of leucosme and melanosome, stromatic-type migmatite.	Recrystallization of Qz around Alm.
SIP18	Migmatite	Kfs, Alm, Qz, Pl, Bt	25	Segregation of leucosme and melanosome, folded stromatic-type migmatite.	Recrystallization of Qz around Alm.
SIP19	Migmatite	Qz, Alm, Kfs, Pl, Bt	35	Segregation of leucosme and melanosome, stromatic-type migmatite.	Recrystallization of Qz around Alm.
SIP20	Migmatite	Qz, Kfs, Alm, Pl, Bt	34	Segregation of leucosme and melanosome, folded stromatic-type migmatite.	Recrystallization of Qz, symplectite mixing of Pl and Kfs.
SIP21	Migmatite	Qz, Kfs, Alm, Pl, Bt, Ilm	30	Very leucratic, segregation unclear.	Recrystallization of Qz, symplectite mixing of Pl and Kfs.
SIP22	Gabbro	Cpx, Pl, Bt	10	Foliated but leucosome not distinct, adjacent to 1 m thick schollen migmatite.	Equigranular, subhedral crystals.
SIP24	Migmatite	Qz, Kfs, Cal, Pl, Cpx, Opx, Bt, Alm	15	Segregation of leucosme and melanosome, stromatic-type migmatite with calcite band.	Recrystallization of Qz, Pl, Cal.
SIP25	Gabbro	Cpx, Hbl, Bt, Pl, Ilm	10	Foliated with thin <2 mm bands of leucosome.	Recrystallization of Qz in leucosome, Cpx and Hbl are equigranular, subhedral crystals.
SIP26	Amphibolite	Hbl, Pl, Ilm	10	No foliation, leucosome not present.	Subhedral to euhedral crystals, low dihedral angles.
SIP43	Migmatite	Alm, Pl, Qz, Kfs, Opx, Ilm, Bt	15	Segregation of leucosme and melanosome, schollen-type migmatite.	Recrystallization of Qz, symplectite mixing of Pl and Kfs.
SIP44	Syenite	Kfs, Opx, Pl, Ilm, Qz	5	Foliated with thin <2 mm bands of Cpx and Hbl.	Some recrystallization of Kfs, Pl, and Qz.

[a]Melt volume initially estimated in the field with a ±5% error and refined via microstructural analysis. SIP20 used as input sample in model results, see section 3. Minerals are listed from largest to smallest volume of sample and abbreviations are from *Whitney and Evans* [2010]: Alm, almandine; Bt, biotite; Cal, calcite; Cpx, clinopyroxene; Hbl, hornblende; Ilm, ilmenite; Kfs, K-feldspar; Opx, orthopyroxene; Pl, plagioclase; and Qz, quartz.

Vp/Vs results for the no fabric model and crystal fabric models are similar (Figure 9, XYZ–5, 6). They remain relatively constant, fluctuating between 1.51 and 1.83 and show a small decrease with higher melt fractions. Prolate ellipsoids in the shape fabric model have similar magnitude results but show an increase to 1.97 Vp/Vs for the highest melt fractions. When oblate melt inclusions and/or melt layers are considered, results indicate that the increase of Vp/Vs2 is overall reflecting an increase in melt fraction, but shows a much higher Vp/Vs than expected for crustal melts of up to 7.52. The layered melt model shows very large Vp/Vs ratios compared to the other models, usually around 30 but up to 57 is observed for Vp/Vs2 in the X_m and Y_m directions. Thus, an increase of Vp/Vs2 is likely to be a good indicator for the presence of melt layers or large aspect ratio ellipsoids. Vp/Vs can be estimated for the whole crust using equation 10 and a typical orogenic crustal section based on *Jamieson et al.* [2011], where there is a 20 km solid upper to middle crust, 2 km partial melt zone and a 15 km solid lower crust. We assume the seismic properties of the solid crust are identical to the solid rocks sampled (Vp = 7.2 km/s, Vs1 = 4.2 km/s, Vs2 = 4.1 km/s). When Vp/Vs is estimated for the whole crust the exaggerated effects of these melt layers are diluted (equation 10). The no fabric model, prolate ellipsoidal melt inclusions in the shape fabric model and crystal fabric models yield a Vp/Vs of 1.73. The Vp/Vs for oblate ellipsoids varies between 1.73 and 1.90 depending on the wave intercept direction. The layered model Vp/Vs of 3.80 is still high for crustal melts.

5. Application to Seismic Data

As expected, seismic velocities reduce in the presence of melt, but this relationship is not linear. Our modeling shows that the reduction depends on the interaction of the melt fraction, melt body size and shape, angle of incidence for seismic waves, and the CPO of the solid phase (Figures 4, 5, and 9). The nonlinear reduction in the seismic velocities at low melt fractions (0–25% melt) is especially noticeable in the shape fabric and layered fabric models (Figure 4). Differences in the reduction of Vs1 and Vs2 result in a varied AVs response when either CPO of the restite or the melt shape is considered (Figures 4 and 9). The seismic wave incidence angle greatly influences seismic wave behavior (Figures 5 and 6). If mineral composition and density as well as the orientation (dip) can be assessed for the suspected partial melt layer/pockets, our models can help to predict more accurate melt volumes. However, if one or more of these parameters are unknown, confidence in predicting melt volumes is significantly reduced and only estimation of location, orientation, and possibly shape is possible [e.g., *Hammond and Kendall*, 2016].

As discussed in section 1, geophysical methods used to determine the presence and volume of melt can yield different predictions (e.g., the Himalaya-Tibet orogen). Vp/Vs from receiver functions is one method commonly used to estimate melt fraction. For example, *Kind et al.* [2002] used teleseismic earthquake records and receiver functions to calculate Vp/Vs, allowing identification of melt accumulations in the Himalaya-Tibet orogen. From the melt models developed in this paper (no fabric, crystal fabric and prolate ellipsoids in the shape fabric model), Vp/Vs is not necessarily very sensitive to melt volume variations. Unless, as is often assumed, melt is oblate or layered, the change of Vp/Vs is minimal and can, in fact, reduce if the melt body is at an angle to the seismic wave propagation direction (Figure 5). Thus, Vp/Vs is unsuitable for prediction of melt volume unless the geometric properties of the melt body can be independently assessed. However, this assessment is rarely made and melt bodies are assumed to be either vertical or horizontal in the crust, depending on the setting of the melt (e.g., magma conduit under a volcano or a migmatitic lower crustal layer, respectively).

In order to illustrate the considerable uncertainty and impact induced by the realistic variation in melt geometries, we compare our model results from this study with the Rayleigh wave velocity reduction (Vs/Vs0) results from *Caldwell et al.* [2009, Figure 10] for the northwest Himalaya. *Caldwell et al.* [2009] measured the dispersion of Rayleigh surface waves and inverted these data to obtain one-dimensional models of shear wave velocity structure. The comparison clearly shows that when geological factors like CPO or melt shape are considered, Vs/Vs0 can vary greatly. *Caldwell et al.* [2009] identified a 7–17% velocity decrease, indicating a 3–7% melt volume. This prediction used the models from *Taylor and Singh* [2002] and *Watanabe* [1993]. *Taylor and Singh* [2002] models horizontal aligned oblate ellipsoids with an $\alpha = 0.1$, we use an α of 0.01 in our models as this is the minimum aspect ratio observed in the field. *Watanabe* [1993] used randomly orientated triangular melt tubes. These models are plotted in Figure 10b together with our models. When the observed results are considered in terms of our models, the crystal fabric model estimates the largest melt volume (15–34%) for the 7–17% Vs reduction observed by *Caldwell et al.* [2009]. However, the layered fabric model estimates a much smaller melt fraction of 1–2% for the same 7–17% Vs reduction. We can therefore explain the 7–17% velocity decrease observed by
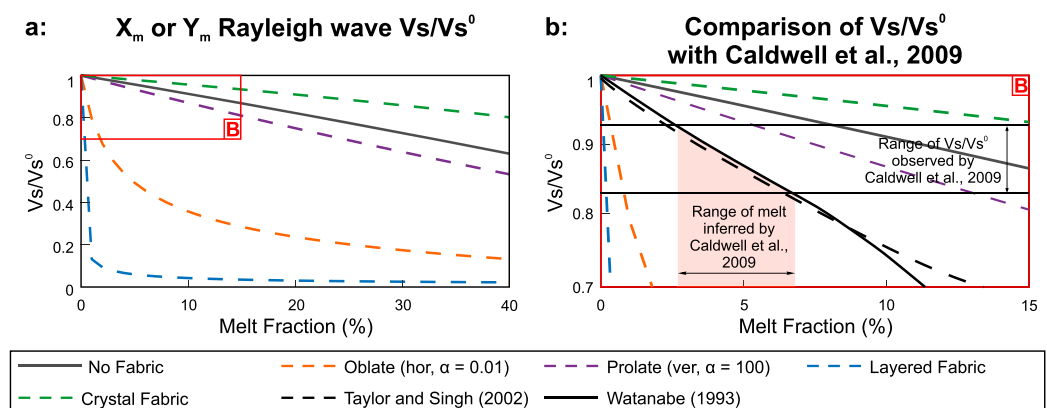
Figure 10. Comparison of modeled velocity reduction with data from *Caldwell et al.* [2009]. (a) Modeled Rayleigh Vs/Vs⁰ for all model variations between 0 and 40% melt in the X1 direction; (b) comparison with *Caldwell et al.* [2009] to show model variations against those calculated by *Taylor and Singh* [2002] and *Watanabe* [1993].

Caldwell et al. [2009] from either much smaller or much larger melt volumes. When the results for Love waves are considered (Figure 5), the effect of isotropic orientated melt on Vs is clear as the layered model yields an 8–18% melt fraction for the 7–17% Vs reduction.

Thus, simultaneous use of Love and Rayleigh waves could help resolve more accurate melt volumes. This comparison emphasizes the importance of the different geological parameters and their effect on seismic properties. Importantly, this simple comparison does not include melt body rotation, which would induce an additional complexity and uncertainty to the seismic behavior. *Hammond and Kendall* [2016] conclude that seismology provides limited constraints on melt volume but can estimate the location, orientation, and possible shape of the melt body. The observations call for robust assessment of the geometric (e.g., melt orientation, Love and Rayleigh wave disparity) and geological (e.g., solid rock and melt shape) properties of the studied crustal volume to aid interpretation of the seismic data.

6. Discussion and Conclusion

Using the experience gained in the present study, future modeling efforts should aim at combining the CPO approach with melt body shapes, orientations, and connectivity. Nevertheless, the models presented here are geologically realistic and can be used to inform geophysical data interpretation and other modeling efforts: the four numerical melt models in this study use real geological data to calculate seismic properties. The solid phase properties and the mesosome (paleomelt) volume are estimated from microstructural analysis and input into the models. The effect of attenuation has not been considered in the paper, in a partially molten rock the important process is melt squirt either between triple junctions [*Mavko and Nur*, 1975; *Mavko*, 1980] or ellipsoidal inclusions [*O'Connell and Budiansky*, 1977]. In both cases, the relaxation time (frequency above which anelastic effects not expected to be significant) is proportional to the melt viscosity. Changing the melt chemistry at 10 Kb from an olivine tholeiite to an andesite increases the viscosity by 1 order of magnitude [*Scarfe et al.*, 1987]. Thus, we can assume the relaxation time also increases by at least an order of magnitude and moving toward the unrelaxed regime [*Faul et al.*, 2004; *Fontaine et al.*, 2008]. This approximation to ignore the anelastic effect is more relevant to crustal melts than less viscous MORB.

The progression of partial melt is assumed to initiate with melt at triple junctions [*Holness*, 2006]. Such very small melt volumes cannot be modeled as spheres or ellipsoids as they are cuspate in shape [*Mavko*, 1980; *Hammond and Humphreys*, 2000a]. *Takei* [2002] modeled the seismic effects of cuspate-shaped melt inclusions, this is a better model for grain scale melt elastic effects than inclusion models. However, anisotropy is not directly addressed due to mineral alignment. The crystal fabric model may be appropriate when melt volume is low and the CPO is the more dominant factor. As melt volumes increase, melt body shape has a much larger impact on the seismic properties; melt may wet grain boundaries [*Garapić et al.*, 2013; but see, *Hiraga et al.*, 2001, 2002] and as volumes increase further, form lenses, layers, and channels, allowing transport of the melt [*Kelemen et al.*, 1997; *Berger and Kalt*, 1999; *Vanderhaeghe*, 2009; *Holness et al.*, 2011]. The transition between small melt pockets and large melt bodies is complex and depends on pressure, temperature, and mineral chemistry. This suggests that oblate ellipsoids in the shape fabric model and layered fabric model are most appropriate analogues for larger melt fractions. However, local geological fabric can be expected to have influence in the spatial orientation of these oblate ellipsoids and layers and they cannot be assumed to be either horizontal or vertical. *Hammond* [2014] shows how back azimuth variations from receiver functions can be used to determine the symmetry axis and thus orientation of melt layers in the crust via anisotropic H-κ stacking. Exposed sections of migmatitic middle and lower crust clearly indicate that nonhorizontal migmatitic layering (e.g., due to shear zone formation or metamorphic dome formation) is a common phenomenon [e.g., *Torvela et al.*, 2013; *Platt et al.*, 2015].

In this paper, we use analytical modeling, based on geological parameters, and a field example to demonstrate that although partial melt greatly affects the seismic response from the middle and lower crust. However, seismic properties do not vary linearly with melt fraction. Mineral composition, shape and alignment of melt, and the solid phase CPO also impact and can result in huge variations of seismic properties. Vp/Vs2 may provide the best constraint for melt volume if it takes the form of layers and oblate ellipsoids. Interpretation of seismic data aiming at quantifying melt percentages or extent of melting should, therefore, always be underpinned by robust modeling of the underlying geological parameters (mineral composition, melt shape, and fabric/melt body orientation with respect to the wave propagation direction) combined with examination of multiple seismic properties in order to reduce uncertainty of the interpretation. Similar effects can be expected to apply to other fluids in the crust.

Table A1. Elastic Moduli of Minerals Used in Modeling Seismic Properties[a]

	ρ	K	G	11	22	33	44	55	66	12	13	23	14	24	34	15	25	35	46	56	Reference
Almandine	3.58	177	94.3	287.4	287.4	287.4	91.6	91.6	91.6	105	105	105									*Babuška et al.* [1978]
Augite	3.4	95.4	59	181.6	150.7	217.8	69.7	51.1	55.8	73.4	72.4	33.9				19.9	16.6	24.6	4.3		*Aleksandrov et al.* [1964]
Biotite	3.06	37.53	15.36	186	186	54	5.8	5.8	76.8	32.4	11.6	11.6									*Aleksandrov and Ryzhova* [1961]
Calcite	2.712	73.3	32	144	144	84	33.5	33.5	33.5	53.9	51.1	51.1	−20.5	20.5						−20.5	*Hearmon* [1979]
Diopside	3.29	108	65.1	204	175	238	67.5	58.8	70.5	84.4	81	57				17	7	43	7.3		*Levien et al.* [1979]
Enstatite	3.19	108	76.8	223	171	216	83	79	87	73	56	50									*Jackson et al.* [1999]
Hypersthene	3.38	102.2	60.7	223	165.4	205.7	83.1	76.4	78.5	70.1	57.3	49.6									*Kumazawa* [1969]
Hornblende	3.12	87	43	116	159.7	191.6	57.4	31.8	36.8	44.9	61.4	65.5				4.3	−2.5	10	−6.2		*Aleksandrov and Ryzhova* [1961]
Ilmenite	3.79	212	132	472	472	382	106	106	152	168	70	70	−27	27		24	−24		−24	−27	*Weidner and Ito* [1985]
K-feldspar	2.56	54	27	62.5	172	124.4	14.3	22.3	37.4	42.8	35.8	24.1				−15.4	−14.3	−11.5	−2.8		*Aleksandrov et al.* [1974]
Quartz	2.65	37.41	44.3	86.8	86.8	105.75	58.2	58.2	39.88	7.04	11.91	11.91	−18.04	18.04						−18.04	*McSkimin et al.* [1965]
Ab$_{62}$-An$_{38}$	2.56	70.7	33.6	96.2	189.4	171.9	23.6	33.1	35.5	46.1	38.4	15.4	5.9	−7	2.2	−0.2	−5.1	7.2	−4.8	1.4	*Aleksandrov et al.* [1974]
Melt	Variable	16.1	0.01	16.1	16.1	16.1	0.01	0.01	0.01	15.967	15.967	15.967									*Rivers and Carmichael* [1987]

[a]C_{ij}, K, and G are in GPa at ambient P, T, and ρ in g/m^3.

Appendix A: Elastic Constants

Here we show the density and elastic moduli for each mineral and the melt phase used to model the seismic properties shown in this paper (Table A1).

References

Akselsen, J. (1982), Precambrian and Caledonian tectonometamorphic evolution of northeastern Seiland, Finnmark, North Norway, *Norg. Geol. Unders. Bull.*, *373*(1977), 45–61.

Aleksandrov, K. S., and T. V. Ryzhova (1961), The elastic properties of rock-forming minerals, I: Pyroxenes and amphiboles, *Izv. Acad. Sci., USSR Geophys. Ser.*, *9*, 1339–1344.

Aleksandrov, K. S., T. V. Ryzhova, and B. P. Belikov (1964), The elastic properties of pyroxenes, *Sov. Phys. Crystallogr.*, *8*, 589–591.

Aleksandrov, K. S., V. V. Alchikov, B. P. Belikov, B. I. Zaslavskii, and A. I. Krupnyi (1974), Velocities of elastic waves in minerals at atmospheric pressure and increasing of precision of elastic constants by means of EVM, *Izv. Acad. Sci., USSR Geophys. Ser.*, *10*, 15–24.

Anderson, D. L. (1989), Elasticity and solid-state geophysics, in *Theory of the Earth*, chap. 6, pp. 103–128, Blackwell Sci., Boston, Mass.

Arzi, A. A. (1978), Critical phenomena melted rocks in the rheology of partially, *Tectonophysics*, *44*(1–4), 173–184, doi:10.1016/0040-1951(78)90069-0.

Babuška, V., J. Fiala, M. Kumazawa, I. Ohno, and Y. Sumino (1978), Elastic properties of garnet solid-solution series, *Phys. Earth Planet. Inter.*, *16*(2), 157–176, doi:10.1016/0031-9201(78)90086-9.

Bachmann, F., R. Hielscher, and H. Schaeben (2010), Texture analysis with MTEX—Free and open source software toolbox, *Solid State Phenomena*, *160*, 63–68, doi:10.4028/www.scientific.net/SSP.160.63.

Backus, G. E. (1962), Long-wave elastic anisotropy produced by horizontal layering, *J. Geophys. Res.*, *67*(11), 4427–4440, doi:10.1029/JZ067i011p04427.

Bass, J. D. (1995), Elasticity of minerals, glasses, and melts, in *Mineral Physics & Crystallography: A Handbook of Physical Constants*, vol. 2, pp. 45–63, American Geophysical Union, Washington, D. C., doi:10.1029/RF002p0045.

Bastow, I. D., S. Pilidou, J.-M. Kendall, and G. W. Stuart (2010), Melt-induced seismic anisotropy and magma assisted rifting in Ethiopia: Evidence from surface waves, *Geochem. Geophys. Geosyst.*, *11*, Q0AB05, doi:10.1029/2010GC003036.

Bauchy, M., B. Guillot, M. Micoulaut, and N. Sator (2013), Viscosity and viscosity anomalies of model silicates and magmas: A numerical investigation, *Chem. Geol.*, *346*(1), 47–56, doi:10.1016/j.chemgeo.2012.08.035.

Berger, A., and A. Kalt (1999), Structures and melt fractions as indicators of rheology in cordierite-bearing migmatites of the Bayerische Wald (Variscan Belt, Germany), *J. Petrol.*, *40*(11), 1699–1719, doi:10.1093/petroj/40.11.1699.

Blackman, D. K., and J.-M. Kendall (1997), Sensitivity of teleseismic body waves to mineral texture and melt in the mantle beneath a mid-ocean ridge, *Philos. Trans. R. Soc. London A*, *355*(1723), 217–231, doi:10.1098/rsta.1997.0007.

Bottinga, Y., and D. F. Weill (1970), Densities of liquid silicate systems calculated from partial molar volumes of oxide components, *Am. J. Sci.*, *269*, 169–182, doi:10.2475/ajs.269.2.169.

Brown, M. (2007), Crustal melting and melt extraction, ascent and emplacement in orogens: Mechanisms and consequences, *J. Geol. Soc.*, *164*(4), 709–730, doi:10.1144/0016-76492006-171.

Brown, M., and G. S. Solar (1998), Shear-zone systems and melts: Feedback relations and self-organization in orogenic belts, *J. Struct. Geol.*, *20*(2/3), 211–227, doi:10.1016/S0191-8141(97)00068-0.

Brown, M., F. J. Korhonen, and C. S. Siddoway (2011), Organizing melt flow through the crust, *Elements*, *7*(4), 261–266, doi:10.2113/gselements.7.4.261.

Caldwell, W. B., S. L. Klemperer, S. S. Rai, and J. F. Lawrence (2009), Partial melt in the upper-middle crust of the northwest Himalaya revealed by Rayleigh wave dispersion, *Tectonophysics*, *477*(1–2), 58–65, doi:10.1016/j.tecto.2009.01.013.

Caldwell, W. B., S. L. Klemperer, J. F. Lawrence, and S. S. Rai (2013), Characterizing the main Himalayan thrust in the Garhwal Himalaya, India with receiver function CCP stacking, *Earth Planet. Sci. Lett.*, *367*, 15–27, doi:10.1016/j.epsl.2013.02.009.

Cornwell, D. G., P. K. H. Maguire, R. W. England, and G. W. Stuart (2010), Imaging detailed crustal structure and magmatic intrusion across the Ethiopian Rift using a dense linear broadband array, *Geochem. Geophys. Geosyst.*, 11, 1–21, doi:10.1029/2009GC002637.

Elvevold, S., H. Reginiussen, E. J. Krogh, and F. Bjørklund (1994), Reworking of deep-seated gabbros and associated contact metamorphism paragneisses in the southeastern part of the Seiland Igneous Province, Northern Norway, *J. Metamorph. Geol.*, 12, 539–556, doi:10.1111/j.1525-1314.1994.tb00041.x.

Eshelby, J. D. (1957), The determination of the elastic field of an ellipsoidal inclusion, and related problems, *Proc. R. Soc. London, Ser. A*, 241(1226), 376–396, doi:10.1098/rspa.1957.0133.

Faul, U. H., J. D. Fitz Gerald, and I. Jackson (2004), Shear wave attenuation and dispersion in melt-bearing olivine polycrystals: 2. Microstructural interpretation and seismological implications, *J. Geophys. Res.*, 109, B06202, doi:10.1029/2003JB002407.

Fontaine, F. R., D. R. Neuville, B. Ildefonse, and D. Mainprice (2008), Influence of melt viscosity of basaltic and andesitic composition on seismic attenuation in partially molten gabbronorite, *Phys. Earth Planet. Inter.*, 167(3–4), 223–229, doi:10.1016/j.pepi.2008.04.010.

Garapić, G., U. H. Faul, and E. Brisson (2013), High-resolution imaging of the melt distribution in partially molten upper mantle rocks: Evidence for wetted two-grain boundaries, *Geochem. Geophys. Geosyst.*, 14, 556–566, doi:10.1029/2012GC004547.

Hammond, J. O. S. (2014), Constraining melt geometries beneath the Afar Depression, Ethiopia from teleseismic receiver functions: The anisotropic H-κ stacking technique, *Geochem. Geophys. Geosyst.*, 15, 1316–1322, doi:10.1002/2013GC005186.

Hammond, J. O. S., and J.-M. Kendall (2016), Constraints on melt distribution from seismology: A case study in Ethiopia, *Geol. Soc. Spec. Publ.*, 420, 127, doi:10.1144/SP420.14.

Hammond, J. O. S., J. M. Kendall, G. W. Stuart, D. Keir, C. Ebinger, A. Ayele, and M. Belachew (2011), The nature of the crust beneath the Afar triple junction: Evidence from receiver functions, *Geochem. Geophys. Geosyst.*, 12, Q12004, doi:10.1029/2011GC003738.

Hammond, W. C., and E. D. Humphreys (2000a), Upper mantle seismic wave velocity: Effects of realistic partial melt geometries, *J. Geophys. Res.*, 105(B5), 10,975–10,986, doi:10.1029/2000JB900041.

Hammond, W. C., and E. D. Humphreys (2000b), Upper mantle seismic wave attenuation: Effects of realistic partial melt distribution, *J. Geophys. Res.*, 105(B5), 10,987–10,999, doi:10.1029/2000jb900042.

Harmon, N., and C. A. Rychert (2015), Seismic imaging of deep crustal melt sills beneath Costa Rica suggests a method for the formation of the Archean continental crust, *Earth Planet. Sci. Lett.*, 430, 140–148, doi:10.1016/j.epsl.2015.07.062.

Hearmon, R. F. S. (1979), The elastic constants of crystals and other anisotropic materials, *Landolt-Börnstein Tables*, 3(11), 1–244.

Henry, P., X. Le Pichon, and B. Goffe (1997), Kinematic, thermal and petrological model of the Himalayas: Constraints related to metamorphism within the underthrust Indian crust and topographic elevation, *Tectonophysics*, 273, 31–56, doi:10.1016/S0040-1951(96)00287-9.

Hiraga, T., O. Nishikawa, T. Nagase, and M. Akizuki (2001), Morphology of intergranular pores and wetting angles in pelitic schists studied by transmission electron microscopy, *Contrib. Mineral. Petrol.*, 141(5), 613–622, doi:10.1007/s004100100263.

Hiraga, T., I. Anderson, M. E. Zimmerman, S. Mei, and D. L. Kohlstedt (2002), Structure and chemistry of grain boundaries in deformed, olivine + basalt and partially molten lherzolite aggregates: Evidence of melt-free grain boundaries, *Contrib. Mineral. Petrol.*, 144(2), 163–175, doi:10.1007/s00410-002-0394-1.

Hirn, A., M. Sapin, J. C. Lépine, J. Diaz, and J. Mei (1997), Increase in melt fraction along a south-north traverse below the Tibetan Plateau: Evidence from seismology, *Tectonophysics*, 273, 17–30, doi:10.1016/S0040-1951(96)00286-7.

Hollister, L. S., and M. L. Crawford (1986), Melt-enhanced deformation: A major tectonic process, *Geology*, 14(July), 558–561, doi:10.1130/0091-7613(1986)14 < 558:MDAMTP>2.0.CO;2.

Holness, M. B. (2006), Melt-solid dihedral angles of common minerals in natural rocks, *J. Petrol.*, 47(4), 791–800, doi:10.1093/petrology/egi094.

Holness, M. B., B. Cesare, and E. W. Sawyer (2011), Melted rocks under the microscope: Microstructures and their interpretation, *Elements*, 7(4), 247–252, doi:10.2113/gselements.7.4. 247.

Holtzman, B. K., and J. M. Kendall (2010), Organized melt, seismic anisotropy, and plate boundary lubrication, *Geochem. Geophys. Geosyst.*, 11, Q0AB06, doi:10.1029/2010GC003296.

Holtzman, B. K., D. L. Kohlstedt, M. E. Zimmerman, F. Heidelbach, T. Hiraga, and J. Hustoft (2003), Melt segregation and strain partitioning: Implications for seismic anisotropy and mantle flow, *Science*, 301(August), 1227–1230, doi:10.1126/science.1087132.

Jackson, I. (2015), 2.21—Properties of pocks and minerals: Physical origins of anelasticity and attenuation in rock, in *Treatise on Geophysics*, vol. 2, 2nd ed., edited by G. Schubert, pp. 539–571, Elsevier, Oxford, U. K.

Jackson, J. M., S. V. Sinogeikin, and J. D. Bass (1999), Elasticity of $MgSiO_3$ orthoenstatite, *Am. Mineral.*, 84, 677–680, doi:10.2138/am-1999-0421.

Jamieson, R. A., M. J. Unsworth, N. B. W. Harris, C. L. Rosenberg, and K. Schulmann (2011), Crustal melting and the flow of mountains, *Elements*, 7(4), 253–260.

Jaxybulatov, K., N. M. Shapiro, I. Koulakov, A. Mordret, M. Landès, and C. Sens-Schönfelder (2014), A large magmatic sill complex beneath the Toba caldera, *Science*, 346, 617–619, doi:10.1126/science.1256785.

Karato, S.-i. (2010), Rheology of the deep upper mantle and its implications for the preservation of the continental roots: A review, *Tectonophysics*, 481(1–4), 82–98, doi:10.1016/j.tecto.2009.04.011.

Karato, S.-i. (2012), *Deformation of Earth Materials: An Introduction to the Rheology of Solid Earth*, Cambridge Univ. Press, Cambridge.

Kelemen, P. B., G. Hirth, N. Shimizu, M. Spiegelman, and H. J. Dick (1997), A review of melt migration processes in the adiabatically upwelling mantle beneath oceanic spreading ridges, *Philos. Trans. R. Soc. London A*, 355(1723), 283–318, doi:10.1098/rsta.1997.0010.

Kind, R., et al. (2002), Seismic images of crust and upper mantle beneath Tibet: Evidence for Eurasian plate subduction, *Science*, 298(November), 1219–1222, doi:10.1126/science.1078115.

Kohlstedt, D. L., M. E. Zimmerman, and S. J. Mackwell (2009), Stress-driven melt segregation in partially molten feldspathic rocks, *J. Petrol.*, 51(1–2), 9–19, doi:10.1093/petrology/egp043.

Krogh, E. J., and S. Elvevold (1990), A Precambrian age for an early gabbro-monzonitic intrusive on the Øksfjord peninsula, Seiland Igneous Province, Northern Norway, *Norsk Geol. Tidsskrift*, 70(4), 267–273.

Kumazawa, M. (1969), The elastic constants of single-crystal orthopyroxene, *J. Geophys. Res.*, 74(25), 5973–5980, doi:10.1029/JB074i025p05973.

Kushiro, I. (1976), Changes in viscosity and structure of melt of NaA1SiO composition at high pressures, *J. Geol.*, 81(35), 6347–6350.

Lejeune, A.-M., and P. Richet (1995), Rheology of crystal-bearing silicate melts: An experimental study at high viscosities, *J. Geophys. Res.*, 100(B3), 4215–4229, doi:10.1029/94JB02985.

Lemonnier, C., F. Perrier, J.-P. Avouac, G. Chitrakar, B. Kalfe, S. Sapkotaj, U. Gautam, D. Tiwari, and M. Bano (1999), Electrical structure of the Himalaya of Central Nepal: High conductivity around the mid-crustal ramp along the MHT, *Geophys. Res. Lett.*, 26(21), 3261–3264, doi:10.1029/1999GL008363.

Levien, L., D. J. Weidner, and C. T. Prewitt (1979), Elasticity of diopside, *Phys. Chem. Miner.*, 4(2), 105–113.

Lin, G., F. Amelung, Y. Lavallee, and P. G. Okubo (2014), Seismic evidence for a crustal magma reservoir beneath the upper east rift zone of Kilauea volcano, Hawaii, *Geology*, *42*(3), 187–190, doi:10.1130/G35001.1.

Lloyd, G. E., R. W. Butler, M. Casey, and D. Mainprice (2009), Mica, deformation fabrics and the seismic properties of the continental crust, *Earth Planet. Sci. Lett.*, *288*(1–2), 320–328, doi:10.1016/j.epsl.2009.09.035.

Lloyd, G. E., R. W. H. Butler, M. Casey, D. J. Tatham, D. Mainprice, and A. Ab (2011a), Constraints on the seismic properties of the middle and lower continental crust, *Geol. Soc. Spec. Publ.*, *360*, 7–32, doi:10.1144/SP360.2.

Lloyd, G. E., J. M. Halliday, R. W. H. Butler, M. Casey, J. Kendall, J. Wookey, and D. Mainprice (2011b), From crystal to crustal: Petrofabric-derived seismic modelling of regional tectonics, *Geol. Soc. Spec. Publ.*, *360*, 49–78, doi:10.1144/SP360.4.

Mainprice, D. (1997), Modelling the anisotropic seismic properties of partially molten rocks found at mid-ocean ridges, *Tectonophysics*, *279*, 161–179, doi:10.1016/S0040-1951(97)00122-4.

Mainprice, D., and M. Humbert (1994), Methods of calculating petrophysical properties, *Surv. Geophys.*, *15*, 575–592, doi:10.1144/SP409.8.

Mainprice, D., R. Hielscher, and H. Schaeben (2011), Calculating anisotropic physical properties from texture data using the MTEX open-source package, *Geol. Soc. Spec. Publ.*, *360*, 175–192, doi:10.1144/SP360.10.

Mainprice, D., F. Bachmann, R. Hielscher, and H. Schaeben (2015), Descriptive tools for the analysis of texture projects with large datasets using MTEX: Strength, symmetry and components, *Geol. Soc. Spec. Publ.*, *409*(1), 251–271, doi:10.1144/SP409.8.

Makovsky, Y., S. L. Klemperer, L. Ratschbacher, and D. Alsdorf (1999), Midcrustal reflector on IDEPTH wide-angle profiles: An ophiolitic slab beneath the India-Asia suture in Southern Tibet?, *Tectonics*, *18*(5), 793–808, doi:10.1029/1999TC900022.

Mavko, G., and A. Nur (1975), Melt squirt in the asthenosphere, *J. Geophys. Res.*, *80*(11), 1444–1448, doi:10.1029/JB080i011p01444.

Mavko, G. M. (1980), Velocity and attenuation in partially molten rocks, *J. Geophys. Res.*, *85*(B10), 5173–5189, doi:10.1029/JB085iB10p05173.

Mckenzie, D. (1984), The generation and compaction of partially molten rock, *J. Petrol.*, *25*, 713–765, doi:10.1093/petrology/25.3.713.

McSkimin, H. J., P. Andreatch Jr., and R. N. Thurston (1965), Elastic moduli of quartz versus hydrostatic pressure at 25° and −195.8°C, *J. Appl. Phys.*, *36*(1965), 1624, doi:10.1063/1.1703099.

Menegon, L., P. Nasipuri, H. Stünitz, H. Behrens, and E. Ravna (2011), Dry and strong quartz during deformation of the lower crust in the presence of melt, *J. Geophys. Res.*, *116*(10), B10,410, doi:10.1029/2011JB008371.

Nábělek, J., G. Hetényi, J. Vergne, S. Sapkota, B. Kafle, M. Jiang, H. Su, J. Chen, and B.-S. Huang (2009), Underplating in the Himalaya-Tibet collision zone revealed by the Hi-CLIMB experiment, *Science*, *325*(5946), 1371–1374, doi:10.1126/science.1167719.

Nelson, K., et al. (1996), Partially molten middle crust beneath Southern Tibet: Synthesis of project INDEPTH results, *Science*, *274*(5293), 1684–1688, doi:10.1126/science.274.5293.1684.

O'Connell, R. J., and B. Budiansky (1977), Viscoelastic properties of fluid-saturated cracked solids, *J. Geophys. Res.*, *82*(36), 5719–5735, doi:10.1029/JB082i036p05719.

Oliver, J. (1962), A summary of observed seismic surface wave dispersion, *Bull. Seismol. Soc. Am.*, *52*(1), 81–86.

Platt, J. P., W. M. Behr, and F. J. Cooper (2015), Metamorphic core complexes: Windows into the mechanics and rheology of the crust, *J. Geol. Soc.*, *172*, 9–27, doi:10.1144/jgs2014-036.

Preston, R. J. (2006), *Magma Density Spreadsheet*. [Available at www.gabbrosoft.org.]

Rivers, M. L., and I. S. E. Carmichael (1987), Ultrasonic studies of silicate melts, *J. Geophys. Res.*, *92*(B9), 9247–9270, doi:10.1029/JB092iB09p09247.

Roberts, D. (1973), Geologisk kart over Norge, berggrunnskart. Hammerfest 1: 250,000, *Norg. Geol. Unders. Bull.*, *61*, 1–49.

Roberts, R. J., F. Corfu, T. H. Torsvik, L. D. Ashwal, and D. M. Ramsay (2006), Short-lived mafic magmatism at 560–570 Ma in the northern Norwegian Caledonides: U-Pb zircon ages from the Seiland Igneous Province, *Geol. Mag.*, *143*, 887–903, doi:10.1017/S0016756806002512.

Rosenberg, C. L., and M. R. Handy (2005), Experimental deformation of partially melted granite revisited: Implications for the continental crust, *J. Metamorph. Geol.*, *23*(1), 19–28.

Rutter, E. H., and D. H. K. Neumann (1995), Experimental deformation of partially molten Westerly granite under fluid-absent conditions, with implications for the extraction of granitic magmas, *J. Geophys. Res.*, *100*(B8), 15,697–15715, doi:10.1029/94JB03388.

Sawyer, E. W., B. Cesare, and M. Brown (2011), When the continental crust melts, *Elements*, *7*(4), 229–234, doi:10.2113/gselements.7.4.229.

Scarfe, C. M., B. O. Mysen, and D. Virgo (1987), Pressure dependence of the viscosity of silicate melts, in *Magmatic Processes: Physicochemical Principles*, vol. 1, 59–67.

Schilling, F. R., and G. M. Partzsch (2001), Quantifying partial melt fraction in the crust beneath the Central Andes and the Tibetan Plateau, *Phys. Chem. Earth, Part A*, *26*(4–5), 239–246, doi:10.1016/S1464-1895(01)00051-5.

Schmeling, H. (1985), Numerical models on the influence of partial melt on elastic, anelastic and electric properties of rocks. Part I: Elasticity and anelasticity, *Phys. Earth Planet. Inter.*, *41*, 34–57, doi:10.1016/0031-9201(85)90100-1.

Sturt, B. A., R. Pringle, and D. M. Ramsay (1978), The Finnmarkian phase of the Caledonian orogeny, *J. Struct. Geol.*, *135*(6), 591–610.

Takei, Y. (2002), Effect of pore geometry on Vp/Vs: From equilibrium geometry to crack, *J. Geophys. Res.*, *107*(B2), 2043, doi:10.1029/2001JB000522.

Takei, Y., and M. Kumazawa (1995), Phenomenological representation and kinematics of general seismic sources including the seismic vector modes, *Geophys. J. Int.*, *121*(3), 641–662, doi:10.1111/j.1365-246X.1995.tb06428.x.

Tandon, G. P., and G. J. Weng (1984), The effect of aspect ratio of inclusions on the elastic properties of unidirectionally aligned composites, *Polym. Composites*, *5*(4), 327–333, doi:10.1002/pc.750050413.

Tatham, D. J., G. E. Lloyd, R. W. H. Butler, and M. Casey (2008), Amphibole and lower crustal seismic properties, *Earth Planet. Sci. Lett.*, *267*, 118–128, doi:10.1016/j.epsl.2007.11.042.

Taylor, M. A. J., and S. C. Singh (2002), Composition and microstructure of magma bodies from effective medium theory, *Geophys. J. Int.*, *149*(1), 15–21.

Teyssier, C., and D. L. Whitney (2002), Gneiss domes and orogeny, *Geology*, *30*(12), 1139–1142, doi:10.1130/0091-7613(2002)030<1139:GDAO>2.0.CO;2.

Torvela, T., J. Moreau, R. W. H. Butler, A. Korja, and P. Heikkinen (2013), The mode of deformation in the orogenic mid-crust revealed by seismic attribute analysis, *Geochem. Geophys. Geosyst.*, *14*, 1069–1086, doi:10.1002/ggge.20050.

Unsworth, M. J., et al. (2005), Crustal rheology of the Himalaya and Southern Tibet inferred from magnetotelluric data, *Nature*, *438*(7064), 78–81, doi:10.1038/nature04154.

Vanderhaeghe, O. (2009), Migmatites, granites and orogeny: Flow modes of partially-molten rocks and magmas associated with melt/solid segregation in orogenic belts, *Tectonophysics*, *477*(3–4), 119–134, doi:10.1016/j.tecto.2009.06.021.

Vanderhaeghe, O., and C. Teyssier (2001a), Partial melting and flow of orogens, *Tectonophysics*, *342*, 451–472.

Vanderhaeghe, O., and C. Teyssier (2001b), Crustal-scale rheological transitions during late-orogenic collapse, *Tectonophysics*, *335*(1–2), 211–228, doi:10.1016/S0040-1951(01)00053-1.

Walker, A. M., and J. Wookey (2012), MSAT-A new toolkit for the analysis of elastic and seismic anisotropy, *Comput. Geosci.*, *49*, 81–90, doi: 10.1016/j.cageo.2012.05.031.

Walker, A. M., A. M. Forte, J. Wookey, A. Nowacki, and J. M. Kendall (2011), Elastic anisotropy of D″ predicted from global models of mantle flow, *Geochem. Geophys. Geosyst.*, *12*, 1–22, doi:10.1029/2011GC003732.

Walsh, J. B. (1969), New analysis of attenuation in partially melted rock, *J. Geophys. Res.*, *74*(17), 4333–4337, doi:10.1029/JB074i017p04333.

Watanabe, T. (1993), Effects of water and melt on seismic velocities and their application to characterization of seismic reflectors, *Geophys. Res. Lett.*, *20*(24), 2933–2936, doi:10.1029/93GL03170.

Wei, W., et al. (2001), Detection of widespread fluids in the Tibetan crust by magnetotelluric studies, *Science*, *292*(5517), 716–719.

Weidner, D. J., and E. Ito (1985), Elasticity of $MgSiO_3$ in the ilmenite phase, *Exp. Tech.*, *40*, 65–70.

Whitney, D. L., and B. W. Evans (2010), Abbreviations for names of rock-forming minerals, *Am. Mineral.*, *95*(1), 185–187, doi:10.2138/am.2010.3371.

Wimmenauer, W., and I. Bryhni (2007), Migmatites and related rocks, in *Metamorphic Rocks: A Classification and Glossary of Terms*, edited by D. J. Fettes, J. Desmons, and P. Árkai, pp. 43–45, Cambridge University Press, Cambridge.

Xie, J., M. H. Ritzwoller, W. Shen, Y. Yang, Y. Zheng, and L. Zhou (2013), Crustal radial anisotropy across eastern Tibet and the Western Yangtze Craton, *J. Geophys. Res. Solid Earth*, *118*, 4226–4252, doi:10.1002/jgrb.50296.